Univerzita Karlova
Přírodovědecká fakulta

Studijní program: Chemie
Studijní obor: Anorganická chemie

Bc. Matěj Nižňanský

Příprava a charakterizace karbidů vybraných d a p prvků
Preparation and characterisation of selected d and p elements carbides

Diplomová práce

Vedoucí práce: RNDr. Václav Tyrpekl, Ph.D.

Praha 2020

Charles University

Faculty of science

Study programme: Chemistry

Branch of study: Inorganic chemistry

Bc. Matěj Nižňanský

Preparation and characterisation of selected d and p elements carbides

Příprava a charakterizace karbidů vybraných d a p prvků

Diploma thesis

Supervisor: RNDr. Václav Tyrpekl, Ph.D.

Prague 2020

Acknowledgement

In memory of my father doc. RNDr. Daniel Nižňanský, Dr.

I would like to thank my supervisor RNDr. Václav Tyrpekl, Ph.D. for his guidance, for the effort he put into helping me become a better scientist *and for the unforgettable mornings with Tom Jones. From now on, I will always know what's new…*

Next, I would like to thank all the people who helped me with the instrumental methods, namely:

Ing. Zdeněk Dlabáček who helped me with the SPS machine

RNDr. Jana Havlíčková for the TG-DTA

Mgr. Petr Brázda, Ph.D. for TEM images

Dr.rer.nat. Mgr. Dominika Zákutná for her help with *polishing* the Rietveld refinement

I would also like to thank Carlos Henrique Vieira Melo, Ph.D. for proofreading and editing this thesis as well as every member of our lab who helped me in any way possible: Ing. Tadeáš Wangle, Ph.D and Mgr. Adam Alemayehu.

Last but definitely not least I would like to thank my girlfriend Zuzana Šťovíčková for her support as well as for the graphic help with this thesis.

Prohlášení:

Prohlašuji, že jsem závěrečnou práci zpracoval samostatně a že jsem uvedl všechny použité informační zdroje a literaturu. Tato práce ani její podstatná část nebyla předložena k získání jiného nebo stejného akademického titulu.

V Praze, 14.06.2020

Podpis

Abstrakt

Tato práce je zaměřena na syntézu karbidových keramických materiálů. Hlavním cílem je syntéza MAX fáze Ti_2AlC za použití roztoků namísto práškové metalurgie. Jako zdroje kovů byly použity chloridy a dusičnany. Jako zdroj uhlíku a zároveň komplexační činidlo sloužila kyselina citronová. Byla nalezena nová cesta syntézy prekurzorů založená na kyselině peroxo-titanové, která umožňuje snížit ztráty hliníku. Syntézy byly prováděny v zařízení pro slinování za asistence elektrického pole, čímž byly zajištěny vysoké rychlosti ohřevu. Podařilo se připravit karbidy jednotlivých prvků Al_4C_3 a TiC a jejich směsi, syntéza fáze Ti_2AlC ale za testovaných podmínek úspěšná nebyla. Fázové složení, struktura a velikost zrn připravených vzorků byla zkoumána metodami práškové rentgenové difrakce, rentgenové fluorescence a elektronové mikroskopie. Obsah uhlíku v prekurzorech byl stanoven termogravimetrickou analýzou.

Klíčová slova: karbid, MAX fáze, roztoková chemie, kyselina citronová, plasmové sintrování, titan, hliník, keramika

Abstract

This thesis is focused on carbide ceramics synthesis, more specifically on the synthesis of a Ti_2AlC MAX Phase carbide using solution chemistry rather than powder metallurgy. Chloride and nitrate precursors have been used as a source of metals and citric acid as a source of carbon for carbothermal reduction and as a complexing agent. A new route of precursor synthesis has been developed based on peroxo-titanic acid, which helps retain aluminium. The syntheses were performed using the SPS facility to ensure high heating rates. Al_4C_3 and TiC carbides and their mixtures were prepared successfully. However, the Ti_2AlC phase was not synthesized under used conditions. The phase composition, structure and grain sizes of the samples were investigated by powder X-ray diffraction, X-ray fluorescence and electron microscopy. The contents of carbon in the precursors were determined by thermogravimetric analysis.

Key words: carbide, MAX Phase, solution chemistry, citric acid, spark plasma sintering, titanium, aluminium, ceramics

Contents

List of used symbols and abbreviations

FAST	Field Assisted Sintering Techniques
SPS	Spark Plasma Sintering
Å	Ångström (10^{-10} m)
HP	Hot Pressing
HIP	Hot Isostatic Pressing
DC	Direct Current
PXRD	Powder X-Ray Diffraction
XRF	X-Ray Fluorescence
SEM	Scanning Electron Microscopy
TEM	Transmission Electron Microscopy
c.a.	citric acid
PTA	Peroxo-titanic acid
BSE	Back-scattered electrons
EDS	Energy-dispersive X-ray spectroscopy
TG-DTA	Thermogravimetry – Differential Thermal Analysis

1 Introduction

MAX Phases are a class of ternary carbides and/or nitrides with inherently laminated structures and consequently anisotropic properties. MAX Phases combine the properties of refractory ceramics (i.e., carbides, nitrides or oxides) and metals, as shown by their high thermal stability and specific stiffness, in addition to good machinability. These materials are used in heating elements, nozzles and electrodes in semiconductors, among other applications, and they may also be used as claddings of 4^{th}-generation nuclear fuel. Accordingly, several patents have been filed on their synthesis [1]–[3] and applications [4]–[6].

MAX Phases are currently synthesized through elemental synthesis. The reagents are processed using hot pressing, spark plasma sintering or molten salt methods. However, each of these syntheses of MAX Phases requires preparing near-ideal mixtures of their precursors, most often by mixing, blending and ball-milling elemental powders in a time- and energy-consuming process.

This process adds additional steps to the synthesis and also requires a high amount of energy. The crushing and ball-milling steps usually take approximately 24 hours and therefore consume much power. Furthermore, the precursor mixture obtained through this process is not perfectly homogenous. Alternately, these limitations in mixing elements in solid state may be overcome by preparing the precursors in solution.

Thus, we aim to prepare such ideal mixtures using solution chemistry instead of powder metallurgy, thereby removing milling steps. For such purposes, water soluble metal salts act as precursors, while using a complexing organic compound as carbon source. The mixture of precursors form metal oxides embedded in a carbon matrix after annealing under inert conditions. These mixtures then yield carbides through carbothermal reduction. This can be done in any vacuum or inert furnace, although a field-assisted sintering techniques (FAST) facility provides faster synthesis times and smaller particle sizes. Therefore, this process would decrease the cost and time of MAX phase synthesis while using inexpensive and easily prepared precursors.

2 Theoretical part

The focus of this research is the synthesis of MAX Phases. These phases are ternary carbides or nitrides. They have similar properties to early-transition metal binary carbides and nitrides but have some crucial differences. To highlight both similarities and differences, binary compounds will be discussed first.

2.1 Early transition-metal carbides and nitrides

Early transition-metal carbides are refractory ceramics commonly used for cutting tools and wear-resistant surfaces. The mechanical and chemical properties of these compounds are similar to those of nitrides because carbon and nitrogen atoms have similar electron structures. However, nitrogen has one more electron than carbon. Thus, the properties of fifth-group nitrides are closer to those of sixth-group carbides than to those of their fifth-group carbide counterparts. These carbides and nitrides share unusual properties that account for their high potential for a wide range of applications. More specifically, they combine the physical properties of ceramics with the electronic properties of metals and therefore are generally very hard and resistant while also displaying high thermal and electrical conductivities [7].

2.1.1 Properties

These carbides are among the hardest materials known, many of which show microhardness values ranging from 2000 to 3000 kg/mm^2, that is, between those of corundum and diamond. For this reason, they are extensively used as cutting tools and wear-resistant surfaces, as mentioned above. In turn, nitrides show slightly lower values of hardness and are consequently less often used for such applications. In addition to their hardness, both early transition-metal carbides and nitrides have very high melting points, typically above 2000 °C, with several examples over 3000 °C. Among these compounds, TaC has the highest melting point (3880 °C), which is comparable to the graphite sublimation temperature (approximately 4000 °C). Furthermore, they are chemically very stable, thereby fitting the definition of refractory materials, as stated in *Refractories Handbook* by C. Schacht [8]: *"Refractory materials by definition are supposed to be resistant to heat and are exposed to different degrees of mechanical stress and strain, thermal stress and strain, corrosion/erosion from solids, liquids and gases, gas diffusion and mechanical abrasion at various temperatures."* All these compounds are refractory, except the 6th group nitrides, which melt or decompose at relatively low temperatures (under 1800 °C) [9].

2.1.2 Synthesis

Early transition-metal carbides are usually synthesized by carbothermal reduction of oxides in hydrogen or argon atmosphere or in vacuum. The powdered reactants are mixed well by ball milling and subjected to hot pressing (HP) or hot isostatic pressing (HIP) at different temperatures. These temperatures vary with each metal and are outlined in Table 2.1. Molybdenum and tungsten carbides are usually synthesized using metal powder instead of oxides although either way is possible for all these metals.

Table 2.1 Temperature ranges of transition-metal carbide synthesis – data retrieved from [7]

carbide	precursors	temperature [°C]	
TiC	TiO_2 + carbon	2000	
ZrC	ZrO_2 + carbon	1800 - 2400	
HfC	HfO_2 + carbon	1800 - 2200	(1600 - 1700)*
VC	V_2O_5 + carbon	1500 - 1700	
NbC	Nb_2O_5 + carbon	1700	
TaC	Ta_2O_3 + carbon	1700	
Cr_3C_2	Cr_2O_3 + carbon	1600	(1300)**
Mo_2C	Mo + carbon	1500	
WC	W + carbon	1400 - 2000	

*using HfH_2 instead HfO_2

**temperatures under 1300 yield Cr_7C_3

Early-transition metal nitrides, in turn, are synthesized using elemental powders, and the reaction is conducted in nitrogen or ammonia atmosphere instead of hydrogen at different temperatures. These temperatures are outlined in Table 2.2.

Table 2.2 Temperature ranges of transition metal nitride synthesis - data retrieved from [7]

nitride	precursors		temperature [°C]
TiN	Ti + NH_3		1200
ZrN	Zr + NH_3		1200
HfN	Hf + NH_3		1200
VN	V + NH_3		1200
NbN	Nb + NH_3		1200
TaN	Ta + NH_3		1200
*AlN	Al_2O_3 + N_2	(Al + NH_3)	800 – 1000
*Si_3N_4	Si + N_2	(Si(NH_2))	1200 – 1400**
*BN	B_2O_3 + NH_3		1200

*although not early-transition metal nitrides, their properties are similar

**for Si + N_2

More recently, binary carbides such as UC [10], HfC [11], VC [12] or WC [13] have also been synthesized using nitrates or chlorides along with organic compounds, for example, citric acid [11], [14], [15], chitosan [16], ascorbic acid [17], phenolic resin [18] or divinylbenzene [19], which are used as carbon sources. These new approaches avoid the need for crushing or ball-milling since the reagents are dissolved and mixed on a molecular level in a solution. This solution is then dried and calcinated under inert conditions to yield a metal oxide imbedded in a carbon matrix. Such a mixture is then treated using the conventional methods described earlier in this section.

2.1.3 Structures of Al and Ti carbides

In this thesis, I aim to synthesize ternary carbides known as MAX phases (further described in chapter 2.2). Binary carbides are intermediate products of this synthesis. Therefore, I also synthesized the carbides that serve as intermediate products of the target MAX phases. This chapter shows the structures (Figure 2.2, Figure 2.4) and properties (Table 2.3; Figure 2.1; Figure 2.3) of the binary carbides synthesized for this purpose.

Table 2.3 Properties of Titanium carbide and Aluminium carbide [20]

		Al_4C_3	**TiC**
space group		R$\bar{3}$m (166)	Fm$\bar{3}$m (225)
cell parameters	a [Å]	3.331	4.31
	b [Å]		
	c [Å]	24.99	
	α [°]	90	90
	β [°]		
	γ [°]	120	
density	[g·cm^{-3}]	2.93	4.93
hardness			9
melting point	[°C]	~2704	3140

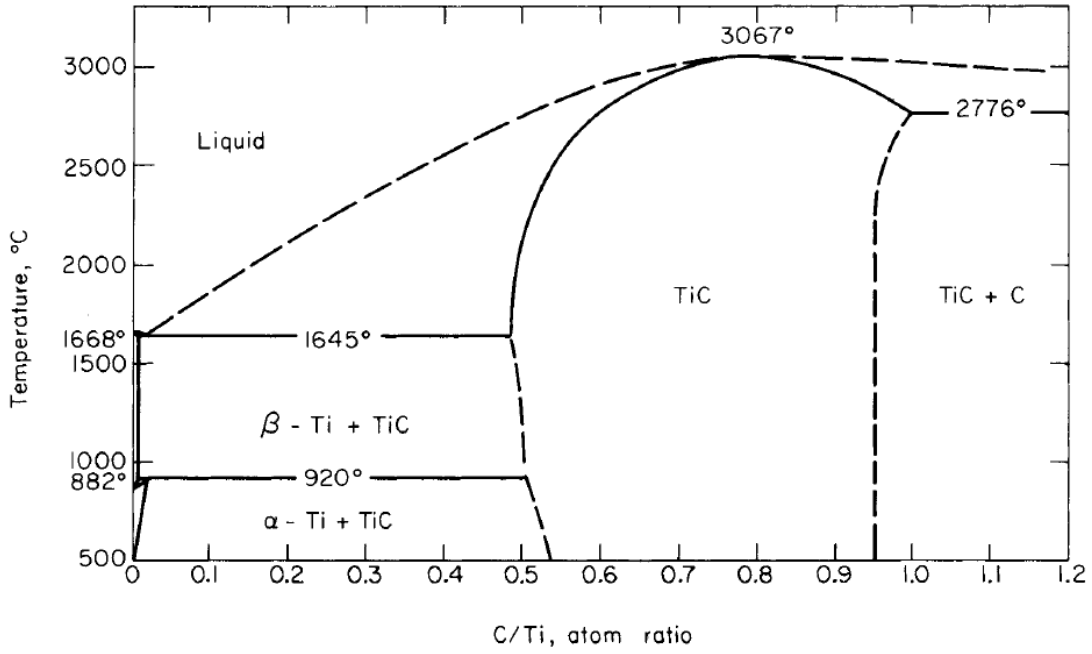

Figure 2.1 Ti-C Phase diagram – retrieved from [21]

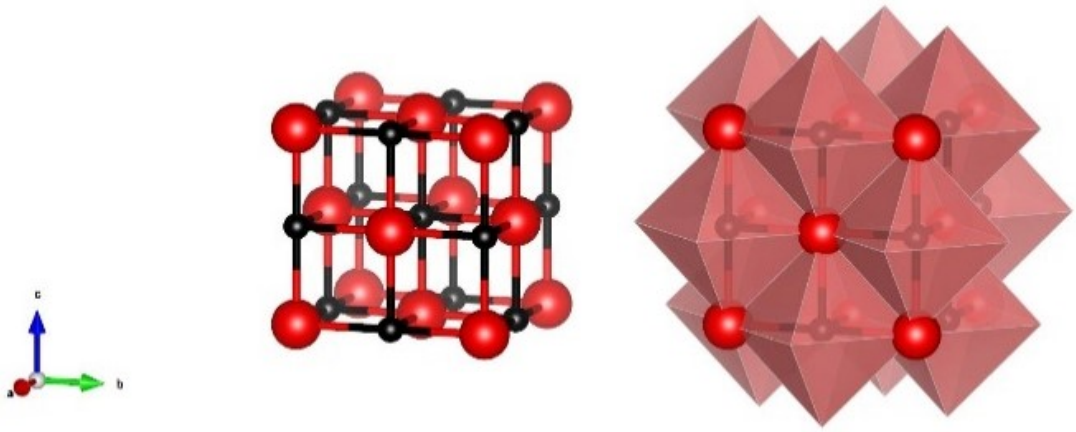

Figure 2.2 Structure of TiC (Ti - red; C - black) Ti_6C octahedra shown in the right [23]

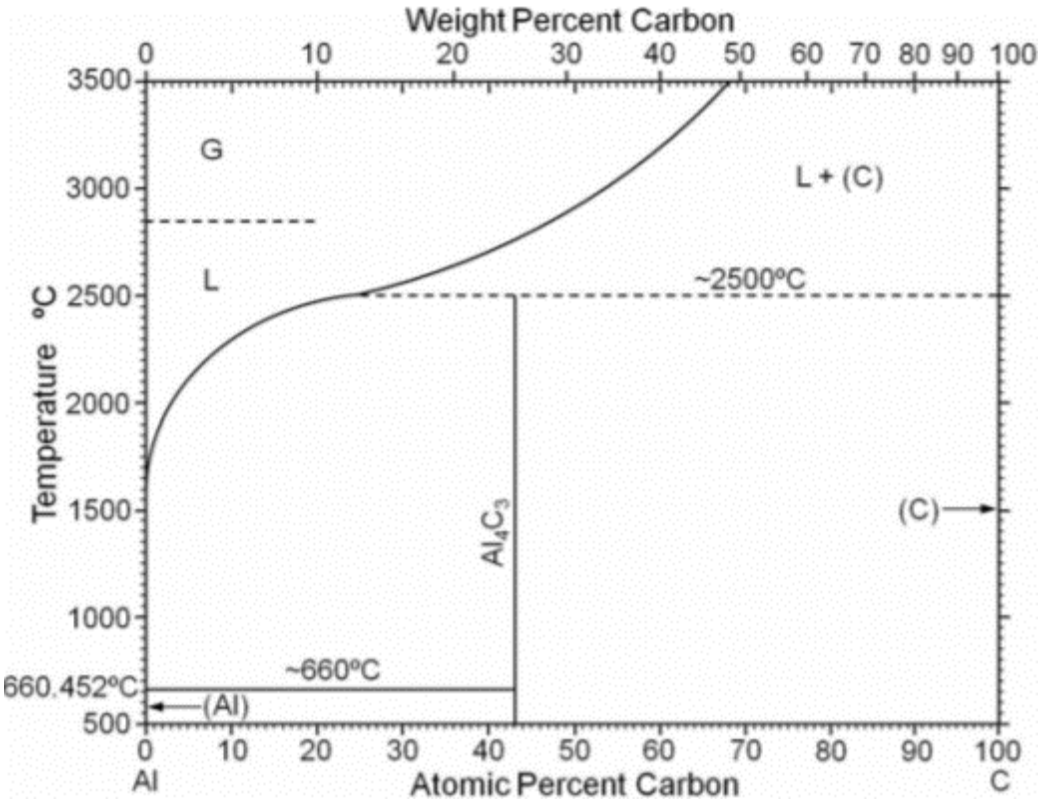

Figure 2.3 Al-C Phase diagram – retrieved from [22]

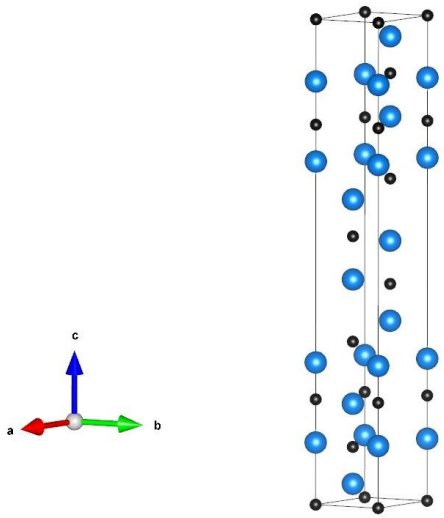

Figure 2.4 Structure of Al_4C_3 (Al - blue; C - black) [23]

2.2 MAX Phases

MAX phases are a group of ternary compounds of general formula $M_{n+1}AX_n$, where M is an early transition metal, A is a p-element, and X is carbon or nitrogen. From the perspective of Materials Science, MAX phases are compounds with a hexagonal structure of the space group $P6_3/mmc$ [24]. Technically, any transitional metal can be an M, and any p-block element can be an A. However, in practical terms, most MAX phases have been synthesized with the M and A elements highlighted in Figure 2.5 in blue and green, respectively.

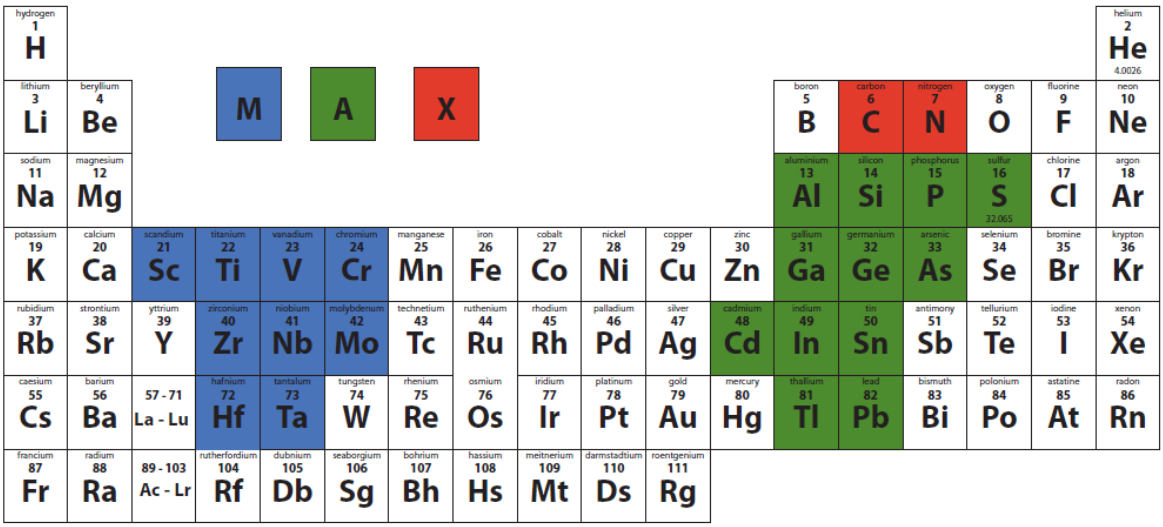

Figure 2.5 Elements used to synthesise known MAX phases – retrieved from [25]

Despite the above, new MAX phases have also been prepared using either other M/A elements or more than one M/A/X element in a solid solution. For example, in 2013, Kuchida et al. prepared Lu_2SnC [26] using lutetium, which is sometimes considered the first transition metal of the 6th period (although lanthanum is more often regarded as such). MAX phases have also been prepared using platinum metals such as copper, gold or iridium as the A element by diffusion in solid state [27], [28]. Nevertheless, MAX phases prepared with these elements have not been studied thoroughly and therefore their potential applications remain unknown.

Concomitantly, a high number of isostructural MAX phase solid solutions have been prepared with more than one M/A/X element. According to Eklund et al. [29], these solid solutions can be classified into M/A-site and X-site solid solutions. M/A-site solid solutions include $(Ti,Cr)_2AlC$, $(Ti,V)_2SC$ and $Ti_3(Si,Al,Ge,Sn)C_2$. The most important X-site solid solutions are MAX carbonitrides with the following general formula: $M_{n+1}A(C,N)_n$ (e.g., $Ti_2Al(C,N)$ or $Ti_3Si(C,N)_2$) [29].

As stated above, the general formula of MAX phases is $M_{n+1}AX_n$. The three usual stoichiometries are referred to as 211, 312 or 413 (for n = 1, 2 or 3 respectively) [29]. In 2010, Zheng et al. synthesized the first 514 MAX phase, $(Ti_{0.5}Nb_{0.5})_5AlC_4$ [30]. The structures of different stoichiometries are shown below (Figure 2.6).

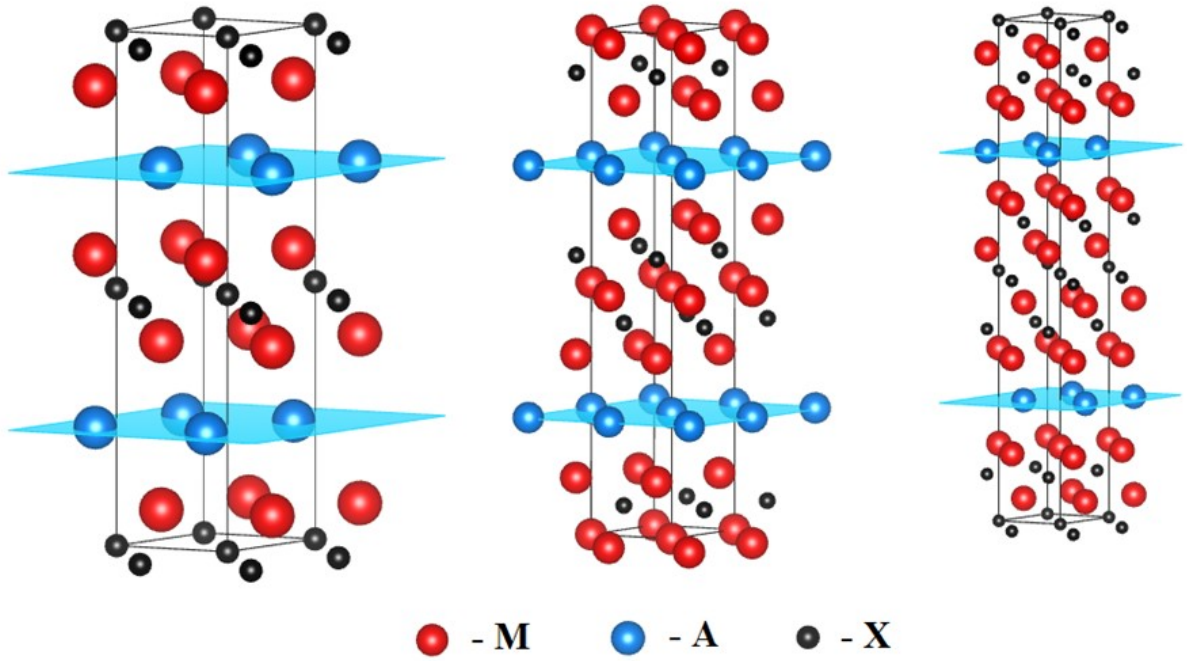

Figure 2.6 Structures of different stoichiometries in MAX phases
Left to right: M_2AX; M_3AX_2; M_4AX_3 [23]

All unit cells presented above in Figure 2.6 consist of M_6X polyhedra and A planes, albeit with different stoichiometries, that is, with two layers of M element for each layer of A element in 211 and with three and four layers of M element in 312 and 413 phases, respectively. Those layers form the aforementioned M_6X polyhedra that share an edge with each other, similarly to binary carbides and nitrides, as shown below in Figure 2.7.

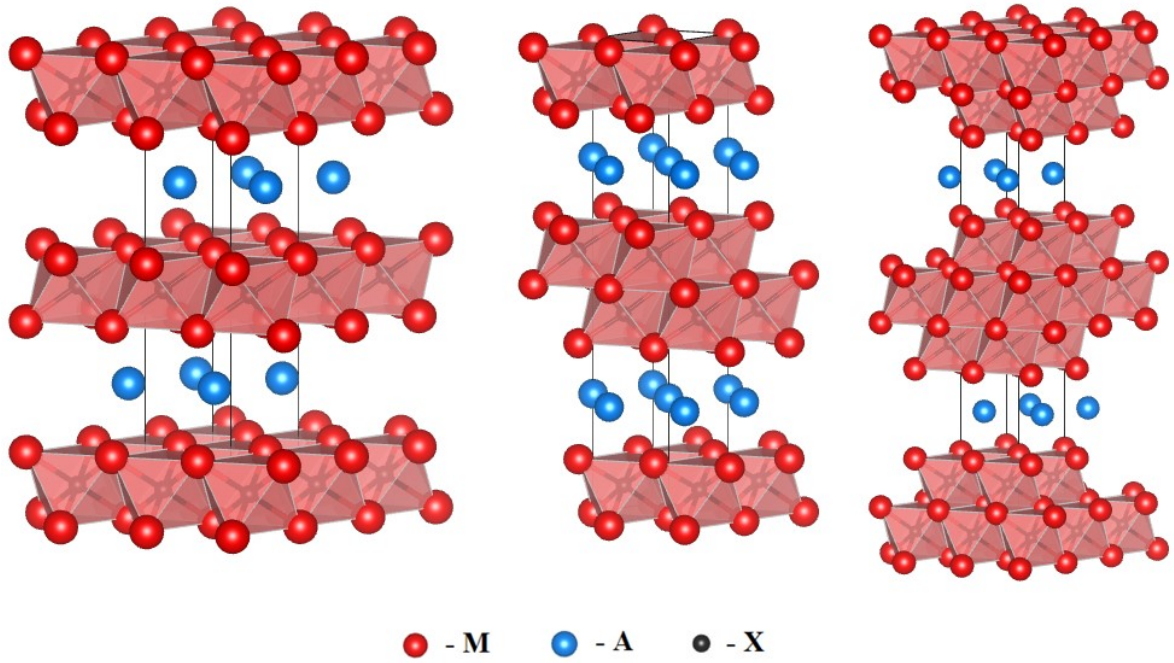

Figure 2.7 M_6X polyhedra in different MAX phases
Left to right: M_2AX; M_3AX_2; M_4AX_3 [23]

The 2 non-equivalent M sites in structures 312 and 413 are usually referred to as M(1) and M(2), and the former forms layers adjacent to A; 413 phases also have 2 non-equivalent X sites: those between two M(2)-layers, referred to as X(1), and those between M(1)- and M(2)-layers, referred to as X(2). The neighbouring MX layers are oriented in such a way that the A layer between them serves as their mirror plane [29], as shown in Figure 2.7.

2.2.1 Properties

2.2.1.1 Thermal stability and decomposition

MAX phases do not melt. They decompose according to the following equation [31]:

$$M_{n+1}AX_n(s) \rightarrow M_{n+1}X_n(s) + A(g\ or\ l)$$

Decomposition starts with the loss of the A element. The removal of A planes generates the twinned structure of $M_{n+1}X_n$ because the A planes serve as mirrors of $M_{n+1}X_n$ layers, as shown in Figure 2.7. Rotation of $M_{n+1}X_n$ layer results in de-twinning into the regular structure of binary nitrides/carbides, as shown in Figure 2.8.

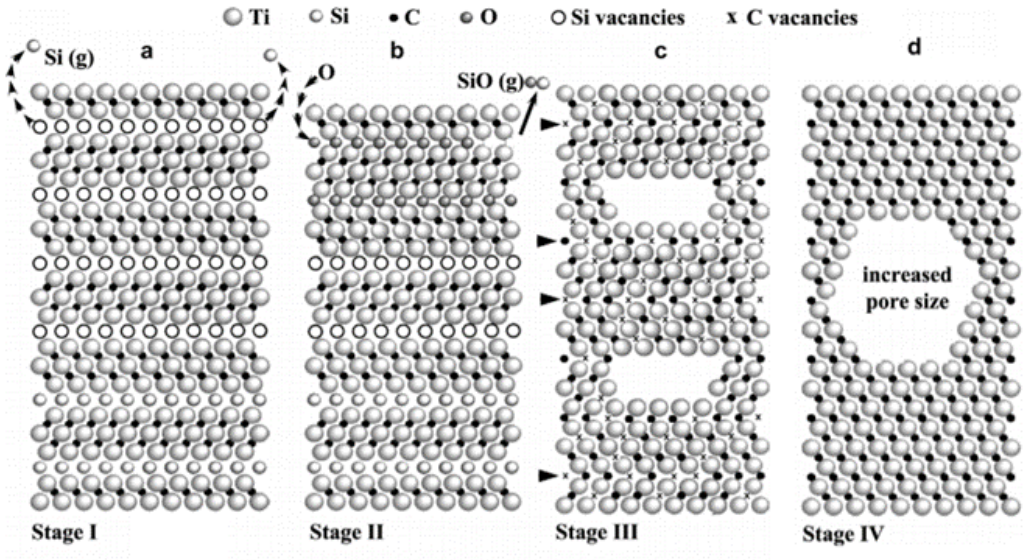

Figure 2.8 Schematic illustration showing different stages of decomposition of Ti_3SiC_2 – Stage I: Si out-diffusion and evaporation; Stage II: O uptake and evaporation of SiO; Ti_3C_2 relaxation, de-twinning, and $TiC_{0.67}$ formation by C redistribution with void formation; Stage IV: $TiC_{0.67}$ layer growth and recrystallisation – adapted from [31]

The reported decomposition temperatures range from 850 °C [32] for Cr_2GaN to 1800 °C [33] for Ti_3SiC_2. However, the thermal stability of MAX phases strongly depends on the environment and on impurities. Hence, their decomposition temperatures may not be determined accurately.

2.2.1.2 Mechanical properties

Bulk MAX Phases have remarkable mechanical properties, including fully reversible dislocation-based deformation and high specific stiffness, in addition to high machinability [29]. The deformation of MAX Phases is a complex process involving a combination of kink and shear band deformation together with delaminations within grains. Bulk Ti_3SiC_2 is

unusually tough, even at room temperature, because various effects, such as microcracking, delamination, grain push-out or grain pull-out, act as energy-absorbing mechanisms during deformation [34]. Their toughness results from their anisotropic structure, which allows mobile basal-plane dislocations at room temperature. As a result, MAX Phases can form kink bands when applying a load [35], as shown in Figure 2.9.

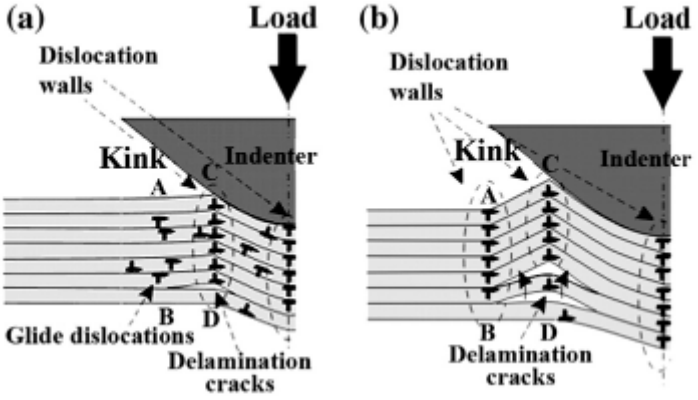

Figure 2.9 Formation of kink bands after applying load – retrieved from [29]

2.2.1.3 Special properties

Farle et al. [25] reported that some M_2AlC (M = Ti; Al; V) phases have self-healing properties once subjected to crack damage.. These cracks are filled with α-Al_2O_3 resulting from selective oxidation. The adhesive energies to the MAX Phase of Al_2O_3 are higher than the cohesive energies between crystal layers of M_2AlC [36].

2.2.2 Synthesis

The method most commonly used for the synthesis of MAX Phases is direct elemental synthesis. In this method, reagents of defined grain sizes are mixed and either crushed in agate mortar or ball-milled. The volatile A elements are usually added in excess (usually approximately 10 %) to compensate for their loss [37]–[39]. Another commonly used method is synthesis using elemental powders and a binary carbide or nitride, e.g., silicon, titanium and titanium carbide or titanium carbide and silicon.

In particular, bulk MAX Phases are usually prepared using hot pressing, spark plasma sintering (SPS) or molten salt methods, among others. In the hot-pressing method, the pellet is loaded into a graphite die and heated to the required temperature (>1000 ˚C) while applying pressure to the sample. The high temperature used in this process requires inert atmosphere to prevent oxidation of the precursors. Ar atmosphere or high-grade vacuum can be used for such purposes. In SPS, the process is almost the same; however, thanks to a different source of heat

(described further in chapter 2.3 below), the heating rates are as high as 1000 but typically around 100 ˚C/min. The SPS method enables us to apply a maximum load ranging from 50 to 250 kN [40]. This method provides complete conversion after 5 minutes of heating but is unsuitable for precursors that produce gaseous side-products in the reaction, such as oxides [10]. In the molten salt method, the inert conditions are ensured by submerging the pellet in a molten salt. This salt is usually either NaCl, KCl, LiCl, KBr or their various mixtures [41]. This method however prevents the application of an external pressure during heating. Regardless of the method used to prepare bulk MAX phases, the precursors are mixed in the desired ratio and ball-milled for extensive periods (~24 h) [42], and the resulting powders are pre-pressed into pellets. However, these pellets are processed differently, depending on the synthesis method.

2.2.3 Applications

MAX phases have been proposed for many applications considering their combined properties. As reviewed by Barsoum et al. [24], these applications include high-temperature structural applications, rotating electrical contacts, bearings, heating elements, nozzles, heat exchangers, tools for die-pressing and impact-resistant materials. In addition, some authors have proposed that Ti_3SiC_2 could be used as radiation-resistant cladding for 4^{th} generation nuclear reactors [43] and as a material for electromagnetic interference shielding [44]. In turn, MAX phases synthesised by sputter-deposition or solid-state reaction can be used as electrodes in SiC-; AlN- or GaN- based semiconductors or sensors [45], [46]. The Ti-Si-C based nanocomposite, which is sold under the name *MaxPhase* is the most common application of a thin-film based on a MAX phase. This type of nanocomposite is widely used in mainstream electrical-contact applications in the telecommunications industry and has a high potential for further applications, such as electrodes in batteries and fuel cells [29].

2.3 Spark plasma sintering

Spark Plasma Sintering (SPS) is a sintering /compaction method that belongs to group of Field-Assisted Sintering Techniques (FAST) [46], [48] This technique is primarily used to compact and sinter materials, but can be used for synthesis as well [49], [50]. Sintering using SPS provides products mostly with better properties than conventional sintering techniques, including higher density, smaller grain size and cleaner grain boundaries. Moreover, this method makes it possible to apply high heating rates, pressure and electric currents [51]. The green body is pressed uniaxially, similarly to the hot-pressing technique (HP), using graphite punches inside a graphite die (as shown in Figure 2.10). However, these methods differ in their heat source. HP requires an external heat source, whereas SPS uses a pulsed DC current. This current flows through the die and the punches, which act as high-power electrical circuit. If the sample is electronically conductive, it also acts as a part of said circuit heating from both the outside and the inside. Moreover, thanks to the good electrical conductivity of these tools, low voltages and therefore high currents are present, thus leading to efficient Joule heat generation. Even electrically non-conductive samples are quickly and efficiently heated by the tooling [40]. The pressing chamber can be evacuated, which enables shorter sintering periods at lower temperatures than HP [52].

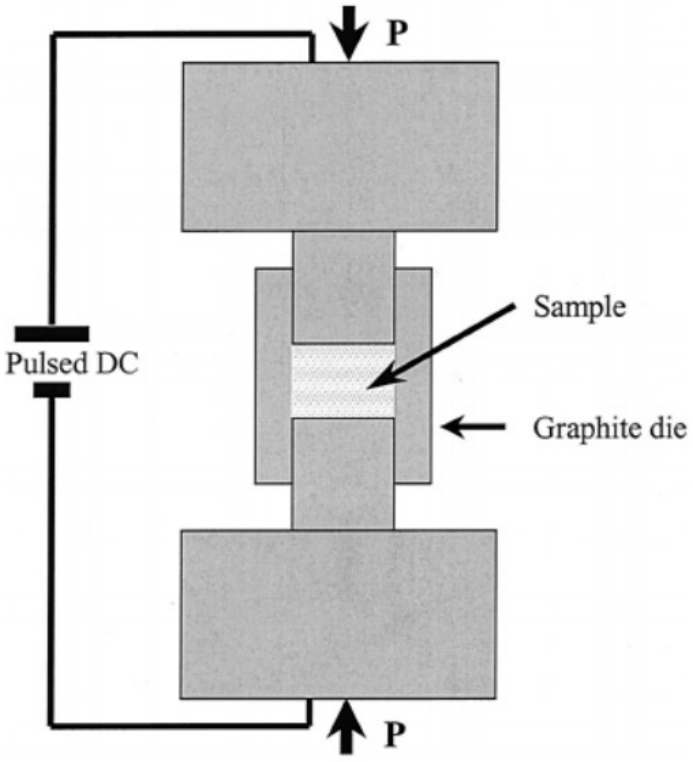

Figure 2.10 Schematic drawing of SPS apparatus - retrieved from [53]

SPS is regarded as a rapid sintering method. The heating power is not only spread over the volume of powder compact but also dissipated at the contact points of the powder particles. Thus, delivering heat exactly where it is required for the sintering process (see Figure 2.11) shortens the sintering times generally to several minutes. Conversely, HP relies on external heating elements using inert gases. Therefore, the sample is heated by conduction from the container. This arrangement leads to slow heating rates with sintering times typically over a few hours and with significant heat losses [54].

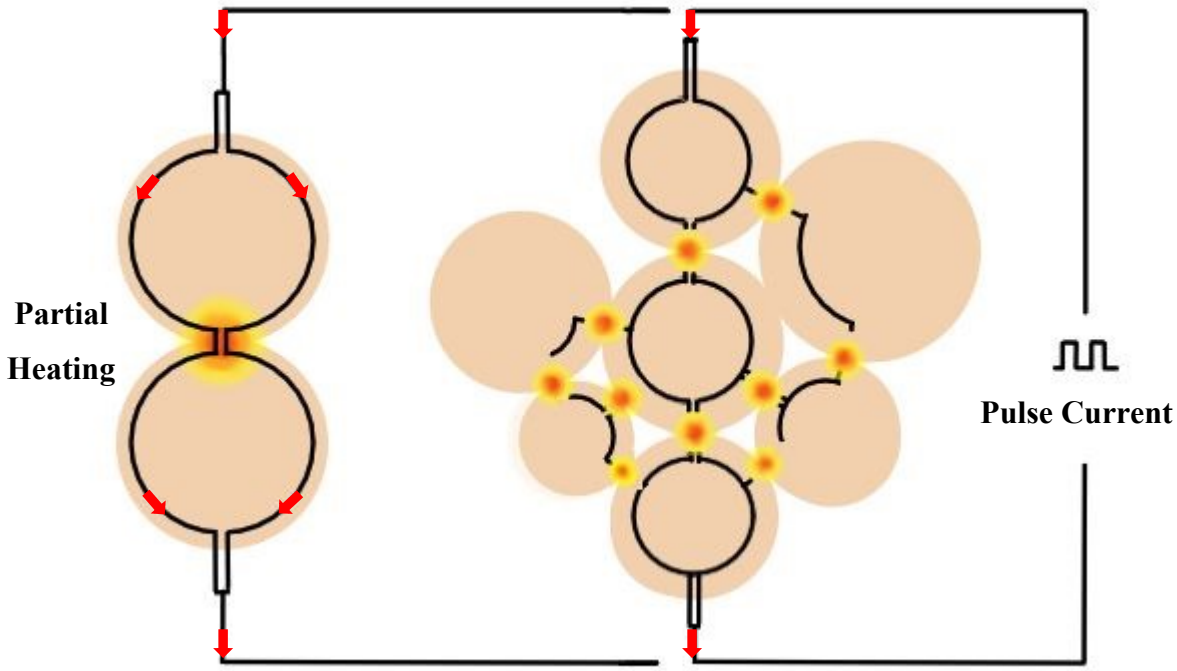

Figure 2.11 Dissipation of energy between the grains at microscopic scale in SPS – adapted from [54]

The presence of plasma in SPS has not been confirmed nor disproved directly by experiments yet. Despite the lack of a direct proof, the presence of occasional electric discharges forming plasma is widely accepted [55].

As mentioned before, the SPS facility can be used solely for synthesis, as a high-power graphite furnace, with the possibility to evacuate the chamber and to use protective atmosphere such as argon. This study uses the facility in such a way.

3 Objectives and outline

The aim of this research is to find a new synthetic route to prepare MAX Phase carbides, which reduces production costs and synthesis time. For such purposes, these carbides will be prepared by carbothermal reduction, albeit with solution chemistry providing excellent metal oxide-carbon mixing. Inexpensive chemicals such as chlorides and nitrates of the relevant metals will be used to maximize the potential of this synthesis for industrial applications. Citric acid will serve as an inexpensive complexing agent and carbon source. Through thermal decomposition of such precursors, a mixture of oxides and carbon will be yielded. This mixture is an ideal precursor for carbide synthesis at higher temperature under inert conditions such as argon atmosphere or high-grade vacuum. In the presence of oxides of multiple elements in the mixture, ternary MAX Phase carbides should be synthesized. The products will be analysed by powder X-Ray diffraction, electron microscopy and X-Ray fluorescence. The phase composition of the products will be determined by Rietveld analysis of X-Ray diffraction data.

4 Experimental part

4.1 Used chemicals

Chemical	Purity	Supplier
$AlCl_3 \cdot 6H_2O$*	99.9 %	Sigma-Aldrich
$TiCl_3$	≥12 % in HCl	Sigma-Aldrich
$TiCl_4$	≥97 %	Merck
Citric acid	≥99.5 %	Sigma-Aldrich
H_2O_2	30 %	Lach-Ner
HNO_3	65 %	Lach-Ner
$Al(NO_3)_3 \cdot 9H_2O$	≥98 %	Sigma-Aldrich
NH_4OH	25 %	Lach-Ner

*dried overnight at 80 °C

Other chemicals were used without further purification

4.2 General synthesis approach

The synthesis will be performed using a process similar to the synthesis of uranium carbide by D. Salvato [10]. Aluminium [56] and titanium [57] citrates will be used as precursors for oxide/carbon nanocomposite synthesis. The resulting composite will then be treated in the SPS facility (used as a fast furnace with reductive environment) for carbothermal reduction. Figure 4.1 shows the outline of the synthesis.

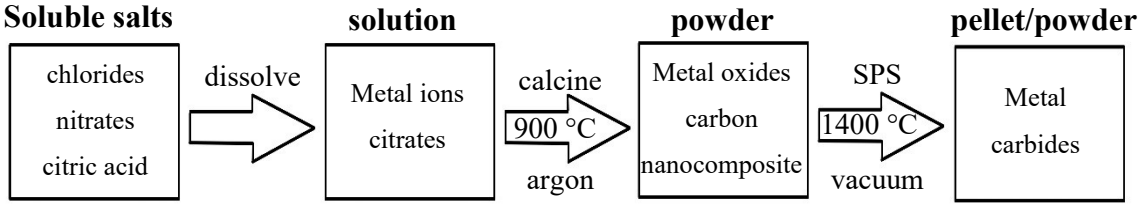

Figure 4.1 Diagram of synthesis approach

4.3 Synthesis of oxide-carbon precursor mixtures

Before Ti_2AlC synthesis, both pure TiC and Al_4C_3 were prepared. Thus, single metal solutions were prepared and treated before the mixed Al/Ti solutions. The first step of the synthesis consisted of decomposing the precursors and citric acid to acquire oxide-carbon mixtures.

4.3.1 Single metal carbide precursors

Oxidic precursors of titanium and aluminium carbides were prepared. The oxides were synthesized from soluble precursors such as chlorides and nitrates, using citric acid as a source of carbon.

First, aluminium trichloride, titanium trichloride and citric acid stock solutions were prepared, using 12% titanium trichloride solution, as purchased. $AlCl_3$ was dissolved in water ($c = 1\ \mathrm{mol \cdot dm^{-3}}$). The citric acid was dissolved in water ($c = 3\ \mathrm{mol \cdot dm^{-3}}$). In the first step, series of solutions for each metal (metal:citrate molar ratios ranging from 1:1 to 1:2) were prepared, as outlined in Table 4.1.

Table 4.1 Series of solutions prepared for oxide synthesis

$n(MCl_3)$ [mmol]	6	6	6	6	6	6	6	6	6	6	6
n(c.a.) [mmol]	6	6.6	7.2	7.8	8.4	9	9.6	10.2	10.8	11.4	12

After evaporating most of the water using a rotary evaporator, the resulting viscous solutions were transferred to annealing boats. The boats were then inserted into a tube furnace equipped with a quartz glass tube (Figure 4.2(a)) fitting four samples, which were thus treated simultaneously. The samples were calcined at 900 °C under a gentle flow of argon (the heating cycle is shown in Graph 4.1).

Graph 4.1 Heating cycle used for oxide synthesis yielding inconsistent amounts of carbon

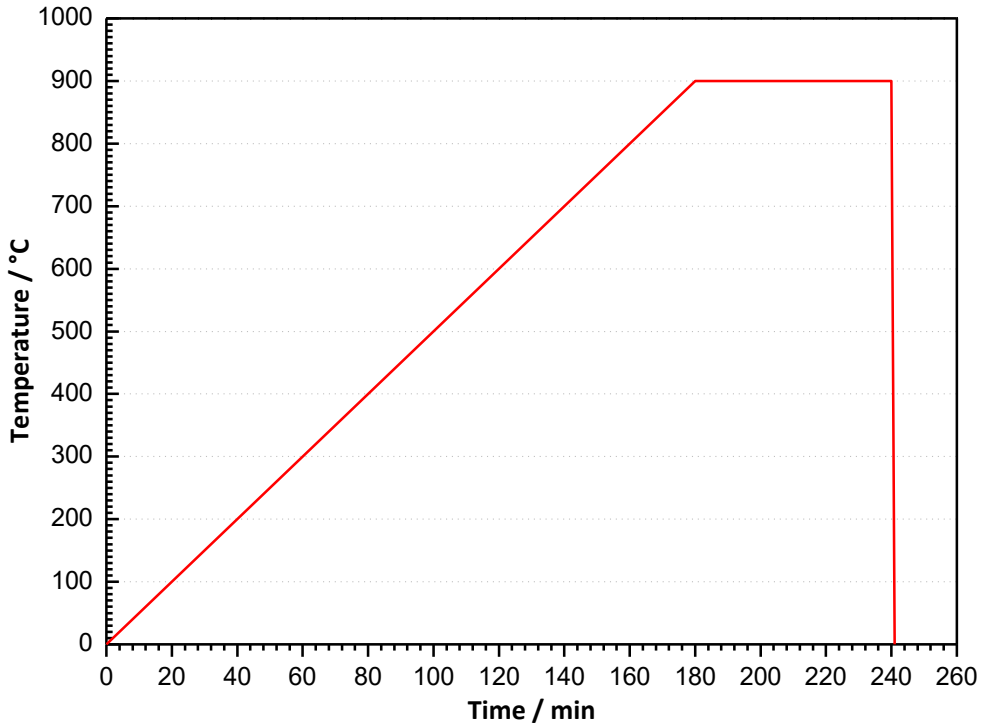

This treatment led to inconsistent amounts of carbon in the final samples, most likely due to citric acid boiling. While some samples were black, others were white, thus indicating that all of the carbon had been oxidized by the remaining air in the setup. To overcome this problem, custom-made, one-way closed quartz glass tubes with a ground joint were used. To ensure consistent results, a series of experiments calcining only solid citric acid were performed while changing both the heating cycles and the experimental setup. In addition to the first setup, two other setups were tried: dynamic vacuum (Figure 4.2(b)) and argon flow after evacuating the tube (Figure 4.2(c)). The latter provided consistent results in carbon derived from the citric acid. As shown in Graph 4.2, the overall heating rate was slowed down to 1 °C/min. Furthermore, the heating was slowed even further to 0.5 °C/min between 280 and 320 °C to make time for citric acid decomposition (~180 - 260 °C [58]) before its boiling point (310 °C). These conditions provided approximately 40 mg (3.33 mmol) of carbon from calcining 1 g (5.20 mmol) of only solid citric acid. This figure might be distorted by gases adsorbed onto annealing boat.

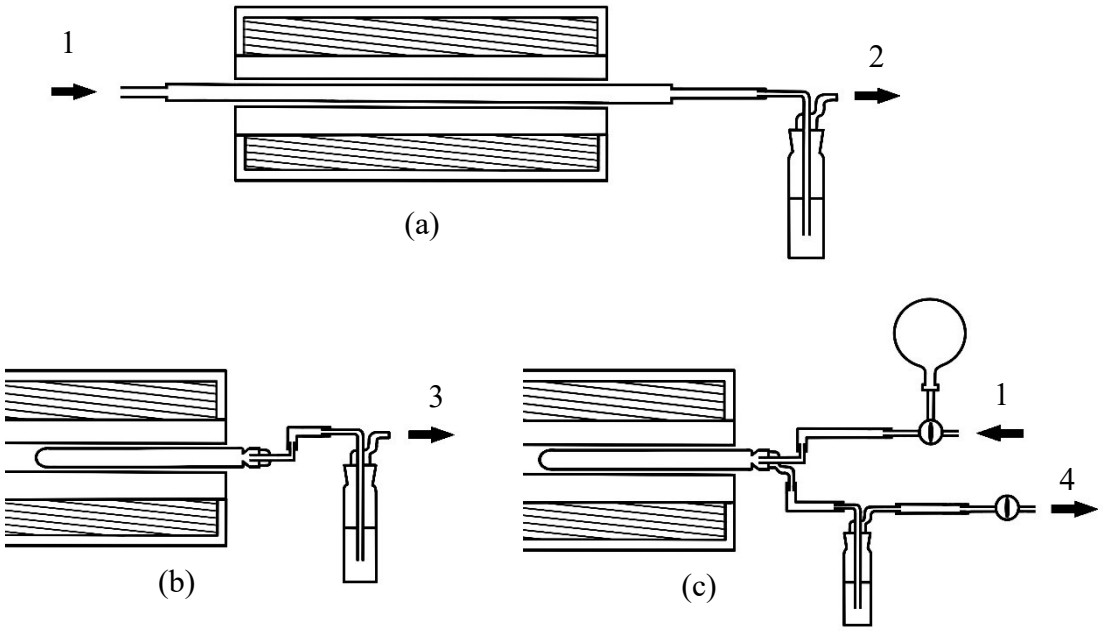

Figure 4.2 Schematics of setups used for calcining the precursors.
(a) gentle argon flow (b) dynamic vacuum (c)argon flow after thorough evacuation
1 – argon in; 2 – argon out; 3 – vacuum; 4 – vacuum or argon out

Graph 4.2 Modified heating cycle used for oxide synthesis yielding consistent amounts of carbon

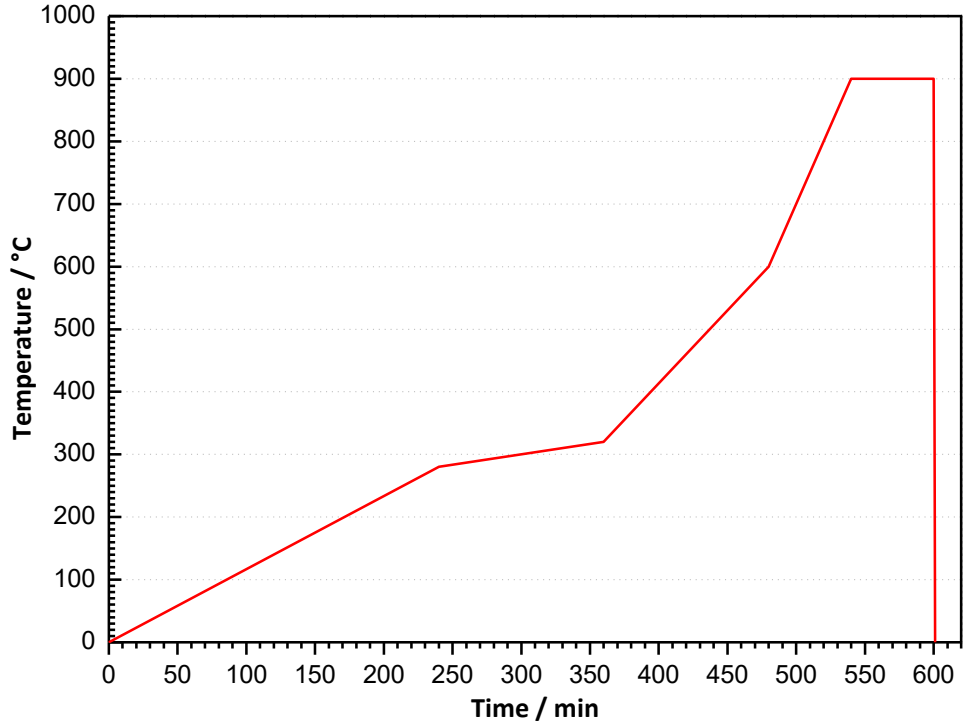

After optimizing the experimental setup with consistent carbon yields, new series of solutions were prepared, as outlined in Table 4.2

These solutions were then annealed using the heating cycle shown in Graph 4.2. This process led to formation of oxide nanoparticles embedded in active carbon. PXRD analysis was performed to identify the products.

Table 4.2 Second series of solutions prepared for oxide synthesis

$n(MCl_3)$ [mmol]	6	6	6	6
n(c.a.) [mmol]	6	7.8	10.2	12

4.3.2 Mixed metals carbide precursors

In the second step, the solutions containing both titanium trichloride and aluminium trichloride with citric acid were prepared, keeping the Ti:Al molar ratio at 2:1 in order to use the mixture of oxides to then synthesize Ti_2AlC. The two-component solution was then subjected to the same treatment as that with single metal solutions. The resulting mixture was analysed by PXRD and XRF. XRF analysis showed that almost no aluminium oxide was present, most likely due to the very low pH of the $TiCl_3$ solution, which must be stabilised with HCl, thereby causing dimerization and subsequent $AlCl_3$ sublimation and thus lowering the aluminium content of the samples.

4.3.3 Mixed metals carbide precursors using titanate route

To overcome the loss of aluminium by evaporation, a new synthesis was conducted. Adapting the synthetic method proposed by Pulišová et al. [59], peroxotitanic acid (PTA) was synthesized as follows: 4 ml of $TiCl_4$ were first hydrolysed to titanium oxide-hydoxide by slow addition into 500 ml of water in a 800ml beaker while stirring vigorously and cooling the reaction in an ice bath. Ammonium hydroxide was then added until the pH value reached approximately 8 to neutralise the HCl formed in the reaction. This suspension was left standing overnight, decanted and washed with water repeatedly to remove any remaining chlorides. The resulting titanium hydroxide was dissolved in H_2O_2, forming a yellow clear solution with a pH value around 2, which gradually turned orange.

$Al(NO_3)_3$ was used as a source of aluminium instead of $AlCl_3$ to prevent loses through dimerization. New solutions with both metals and different metal:citrate ratios were prepared, as outlined in Table 4.3. The solutions were evaporated, using a rotatory evaporator, forming a very viscous clear slightly yellow solution, which started to turn into gel after a couple of hours. The powders resulting from annealing were analysed by PXRD to rule out any crystallisation. The analysis showed that the resulting powders were amorphous. The samples were then calcinated using the same treatment as that with single metal solutions. The resulting mixture was analysed by PXRD and XRF.

Table 4.3 Series of solutions used for synthesis of $Al_2O_3/TiO_2/C$ mixtures

$n(Al(NO_3)_3)$ [mmol]	6	6	6	6
n(PTA)	12	12	12	12
n(c.a.) [mmol]	18	24	30	36

4.4 High temperature treatment of precursors in SPS facility

Carbides of titanium and aluminium were prepared before attempting full MAX Phase synthesis. The carbides were synthesized using mixtures of oxide nanocrystals embedded in carbon synthesized in the previous step (see section 4.34.3.1), inside the SPS facility.

4.4.1 Single metal carbide synthesis

The powders were first pre-compressed at approximately 110 MPa using a hand press. The resulting pellets, which were not self-supporting and crumbled easily, were put into custom-

made hollow graphite punches (see Figure 4.3) interlaced with graphite foil to allow gases formed during the carbothermal reduction to escape.

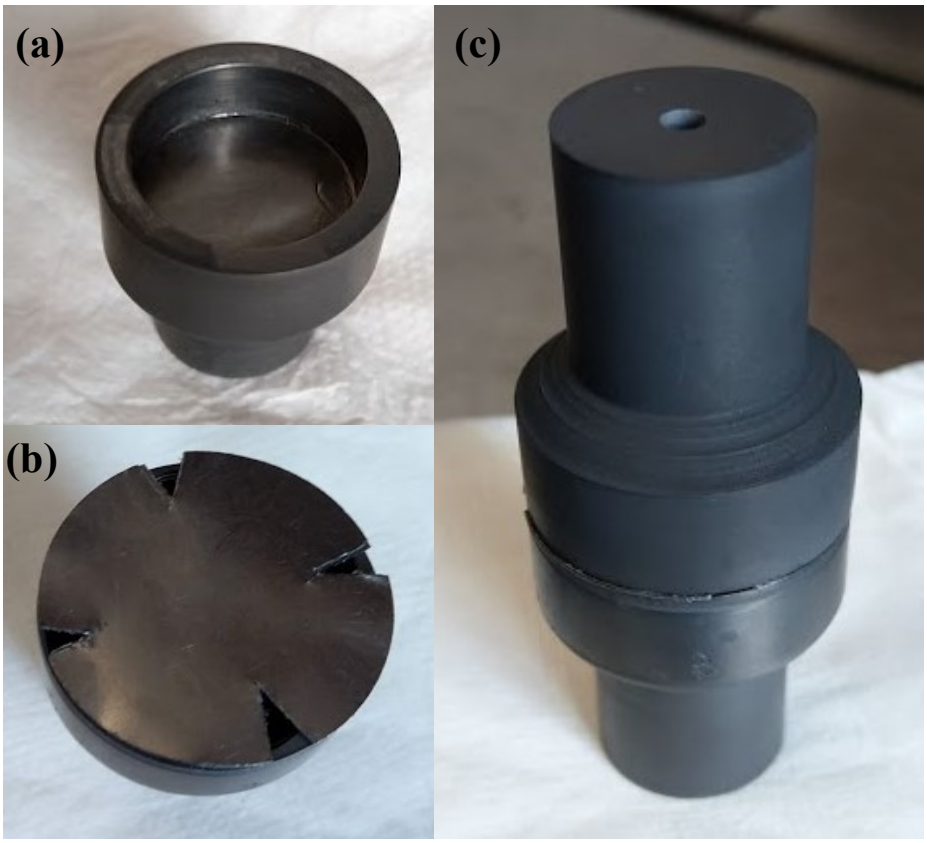

Figure 4.3 (a) used custom-made punch; (b) interlacing graphite foil; (c) set of both punches

The punches were then put into the SPS machine, which was evacuated to a pressure of approximately 10 Pa (1 atm of Ar was used in one case to assess the effect of low pressure on the reaction). The samples were heated at the rate of 200 °C/min with a dwell time of 20 minutes. The contact pressure on the punches was set to 5 MPa without applying pressure on the sample.

4.4.2 Mixed metals carbide synthesis

The reactions were conducted using the mixture mentioned in previous step (see section 4.3.3) in the SPS machine. The resulting powders and pellets were analysed by PXRD and SEM.

4.5 Summary of selected samples

The following tables provide an overview of the main samples analysed in this study. Table 4.4 summarises the precursor samples (intermediate step, calcined at 900°C to yield an oxide/carbon nanocomposites). Table 4.5 outlines the samples fired in the SPS facility to high temperature

Table 4.4 Overview of selected precursor samples

Sample	Obtained phases	note
1	Al_2O_3 + C	Prepared from $AlCl_3$ + citric acid (ratio 1:1)
2	TiO_2 + C	Prepared from $TiCl_3$ + citric acid (ratio 1:1)
3	TiO_2 + Al_2O_3 + C	Prepared from $TiCl_3$ + $AlCl_3$ + citric acid (ratio 2:1:3) almost no aluminium present
11	TiO_2 + Al_2O_3 + C	Prepared from $Al(NO_3)_3$ + PTA + citric acid (ratio 2:1:6) calcined as a solution
12	TiO_2 + Al_2O_3 + C	Prepared from $Al(NO_3)_3$ + PTA + citric acid (ratio 2:1:6) calcined as a gel

Table 4.5 Overview of selected carbide samples

Sample	Obtained phases	note
5	Al_4C_3	Prepared from sample 1 (1500 °C, vacuum, 20 min)
6	Al_4C_3	Prepared from precursor similar to sample 1 (ratio 1:1.3) (1500 °C, vacuum, 20 min)
7	Al_4C_3	Prepared from precursor similar to sample 1 (ratio 1:1.7) (1500 °C, vacuum, 20 min)
8	Al_4C_3	Prepared from precursor similar to sample 1 (ratio 1:2) (1500 °C, vacuum, 20 min)
9	TiC	Prepared from sample 2 (1500 °C, vacuum, 20 min)
10	TiC	Prepared from sample 3 (1500 °C, vacuum, 20 min)
13	Al_4C_3 + TiC*	Prepared from sample 11 (1400 °C, vacuum, 20 min)
14	Al_2O_3 + TiC*	Prepared from sample 11 (1400 °C, argon, 20 min)
15	TiC*	Prepared from sample 12 (1100 °C, vacuum, 20 min)
16	TiC*	Prepared from sample 12 (1200 °C, vacuum, 20 min)
17	TiC*	Prepared from sample 12 (1300 °C, vacuum, 20 min)
18	Al_4C_3 + TiC*	Prepared from sample 12 (1400 °C, vacuum, 20 min)

*expected to contain amorphous phases undetectable by PXRD

4.6 Instrumental Techniques

4.6.1 Powder X-ray diffraction

Powder X-ray diffraction (PXRD) was performed on a PANalytical X'pert PRO system using a CuK_α lamp ($\lambda = 1.5418$ Å) with a secondary monochromator and a PIXcel position-sensitive detector at the Faculty of Science, Charles University in Prague.

The samples were measured in 2θ range of 10° to 100° or 10° to 80°, setting the spinner stage to 2 seconds per revolution. The results were analysed with X'Pert HighScore [60] using the Search-Match function and the PDF cards of the samples. Rietveld analysis was performed using WinPLOTR [61] software with Thompson-Cox-Hastings pseudo-Voigt peak shape function. The grain sizes (τ) were calculated using the Scherrer formula

$$\tau = \frac{\kappa \cdot \lambda}{\beta \cdot cos\theta},$$

where κ is a shape factor (0.9), λ is used x-ray wavelength (Cu k_α), β is the measured line broadening and θ is the Bragg angle.

4.6.2 Scanning Electron Microscopy

The morphology of the final powders was studied under scanning electron microscopes JEOL JSM-6510 at the Institute of Inorganic Chemistry of the Czech Academy of Sciences in Řež. The samples were coated with a thin Au/Pd layer.

4.6.3 Transmission Electron Microscopy

Transmission electron micrographs were acquired at the Department of Structure Analysis Institute of Physics, Czech Academy of Sciences in Prague, on a FEI Tecnai G2 20 microscope operating at 200 kV with an LaB_6 cathode equipped with an Olympus SIS Veleta CCD camera (14 bit). The powder was ground and suspended in isopropanol, and a drop was deposited on Cu holey-carbon TEM grid.

4.6.4 Spark Plasma Sintering

Synthesis was conducted on a Model SPS 10-4 10 Ton machine by Thermal Technology LLC (USA) at the Institute of Plasma Physics, Czech Academy of Sciences, in Prague, with the following specifications: 10 t maximum pressure load, 4000 A maximum DC heating current at 10 V (40 kW heating power). The temperature was measured using a pyrometer in the measuring range from 600 to 2200 °C directed at the middle of the die. All graphite parts were made of SIGRAFINE R8710 (SGL Group).

The samples were placed in the cavity of custom-made punches without using the die. The SPS chamber was evacuated using a two-stage rotary pump (ca. 4 Pa). The process was controlled using a Eurotherm 2704 regulator with two independent outputs for temperature and pressure control, controlled by the iTools Engineering software. The process was monitored using SpecView software, recording the measurements in 1s intervals.

4.6.5 X-ray fluorescence

The XRF measurements were conducted on a Rigaku NEX CG energy dispersive fluorescence spectrometer with Rh 50W X-ray source at the Faculty of Science, Charles University, in Prague. For higher accuracy, the spectrometer contains four targets that modify the energy of the radiation: RX9 for the characteristic radiation between 1.0 and 2.8 keV, Cu for radiation between 3.0 and 8.0 keV, Mo between 6 and 15 keV and Al between 16 and 38 keV.

The powder samples were loaded into a cuvette and pressed at a torque of approximately 20 N · m. The usual amount of sample ranged from 200 to 400 mg. Samples were measured in the helium atmosphere and evaluated using NEX software.

The analyses were conducted using a standardless method; therefore, the values may not be precise, with errors of units of percent. Accordingly, the element ratios may be unreliable.

5 Results and discussion

5.1 Active carbon-oxide prcursor nanocomposites

Oxides embedded in a carbon matrix were synthesized in the first step of the process (see Figure 5.1). The mixtures of oxides were usually amorphous and could not be characterised by PXRD.

Figure 5.1 TiO_2/carbon precursor nanocomposite (sample 2)

5.1.1 Single metal oxide/carbon precursors

In order to prepare binary carbides, the metal citrates were calcined, which resulted in mixtures of Al_2O_3 (alumina) or TiO_2 (titania) with carbon. A series of four samples was prepared for each metal. Those samples varied only in the relative content of carbon, which depended on the amount of citric acid used for synthesis, turning into black powders after annealing. In the case of Ti, thermogravimetric analysis (Graph 5.2) showed that the Ti:C ratio after calcination was 0.83; that is, in comparison to the original ratio of 1, approximately 1.2 moles of carbon were formed per mole of citric acid.

In turn, the Al system (Graph 5.1) had a Al:C ratio of 0.23; that is, in comparison to the original ratio of 1, approximately 4.4 moles of carbon were formed per mole of citric acid. Since the carboxyl groups in c.a. will come off as CO_2, no more than three carbon atoms can be expected to form per single citric acid molecule. The Al/C ratio after thermal decomposition is, however, more than three times higher than the initial Al/c.a. ratio. This suggests that some Al was lost during thermal decomposition.

Graph 5.3 shows the diffraction pattern of the Al_2O_3/carbon precursor nanocomposite (sample 1). The diffraction lines of Al_2O_3 (indicated in the graph) are not well developed above the background, thus indicating that any Al present is in amorphous form.

Graph 5.4 shows the diffraction pattern of TiO_2/carbon precursor nanocomposite (sample 2). Based on the diffraction pattern, titania is present as a crystalline mixture of rutile (24.9 %) and anatase (75.1 %). The average apparent sizes of crystallites were 22.8 nm for anatase and 67.2 nm for rutile. With the increase in the relative content of citric acid, PXRD showed a decrease in peak intensity of the crystalline phases (Graph 5.5) and significant peak broadening (detail in Graph 5.6), which indicates that the precursors were homogenous and that the increase in carbon content caused a decrease in particle sizes.

Graph 5.1 TG-DTA of Al_2O_3/C precursor nanocomposite (sample 1)

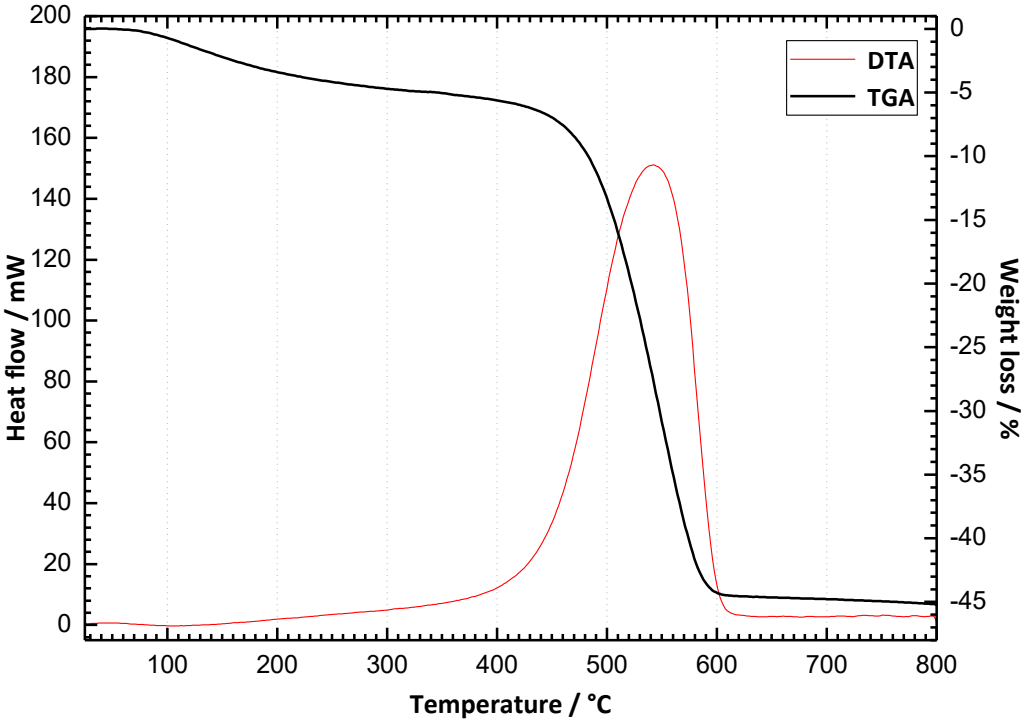

Graph 5.2 TG-DTA of TiO_2/C precursor nanocomposite (sample 2)

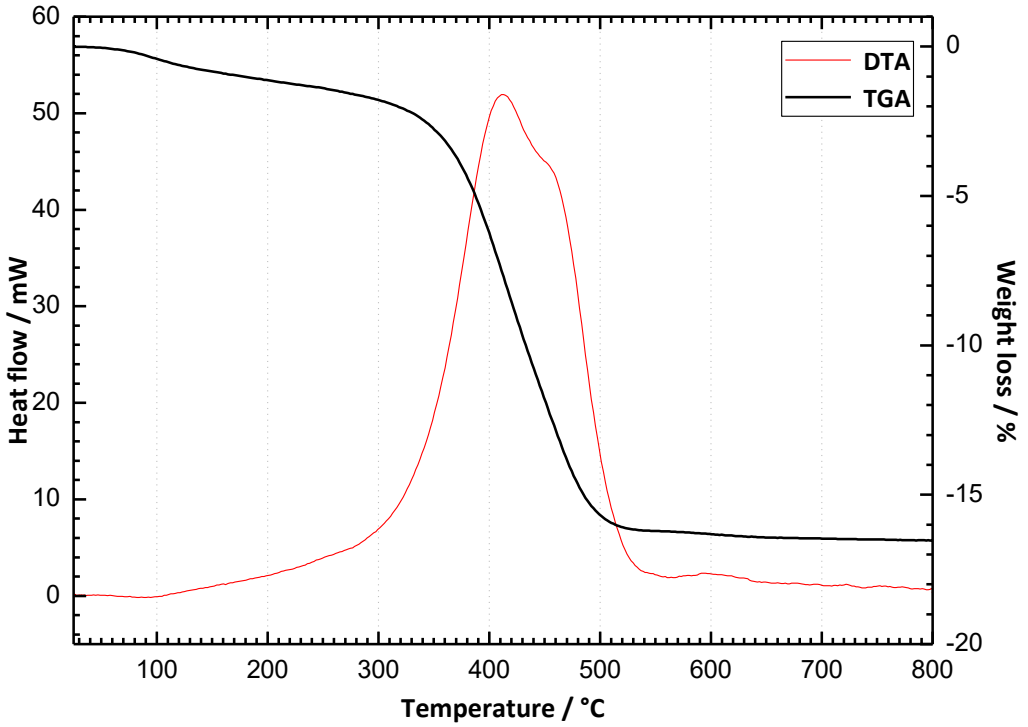

Graph 5.3 Diffraction pattern of Al_2O_3/C precursor nanocomposite (sample 1) – no crystalline phase was observed. Expected Al_2O_3 phase was added to demonstrate that none of its peaks is present

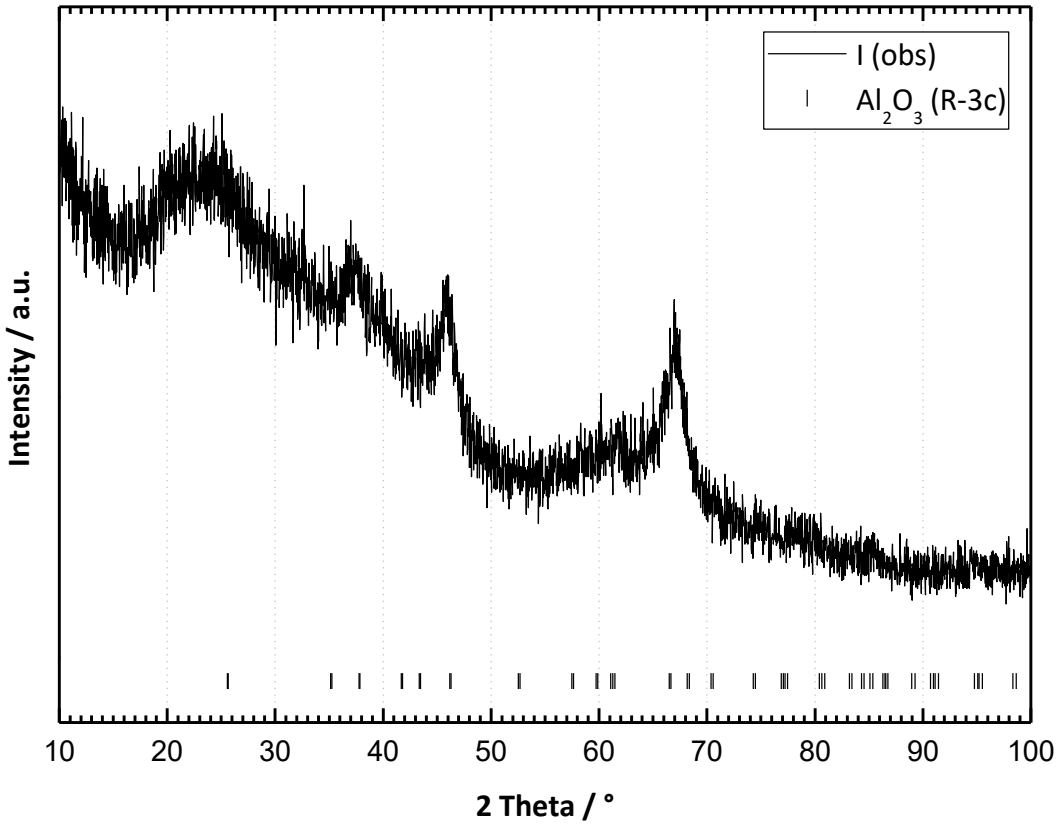

Graph 5.4 Diffraction pattern of TiO_2/C precursor nanocomposite (sample 2) – a mixture of rutile and anatase.

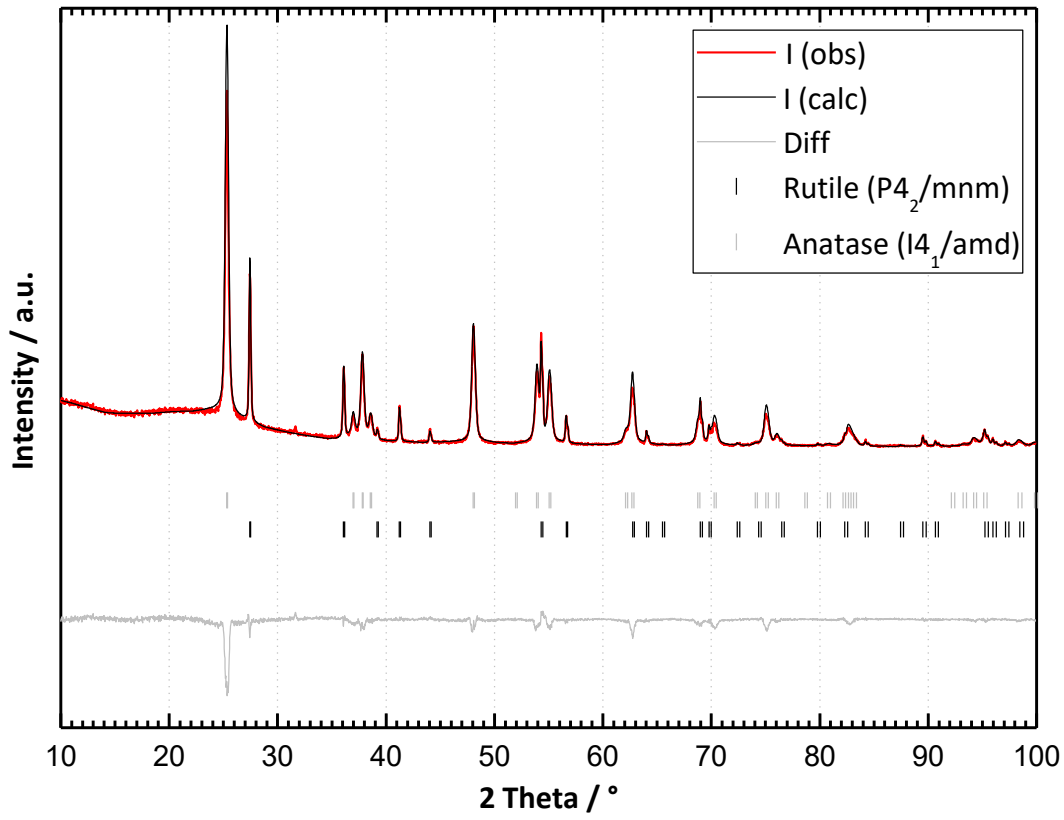

Graph 5.5 Comparison of diffraction patterns of TiO_2/C precursor nanocomposites for different Ti:c.a. ratios (0.1 - 2)

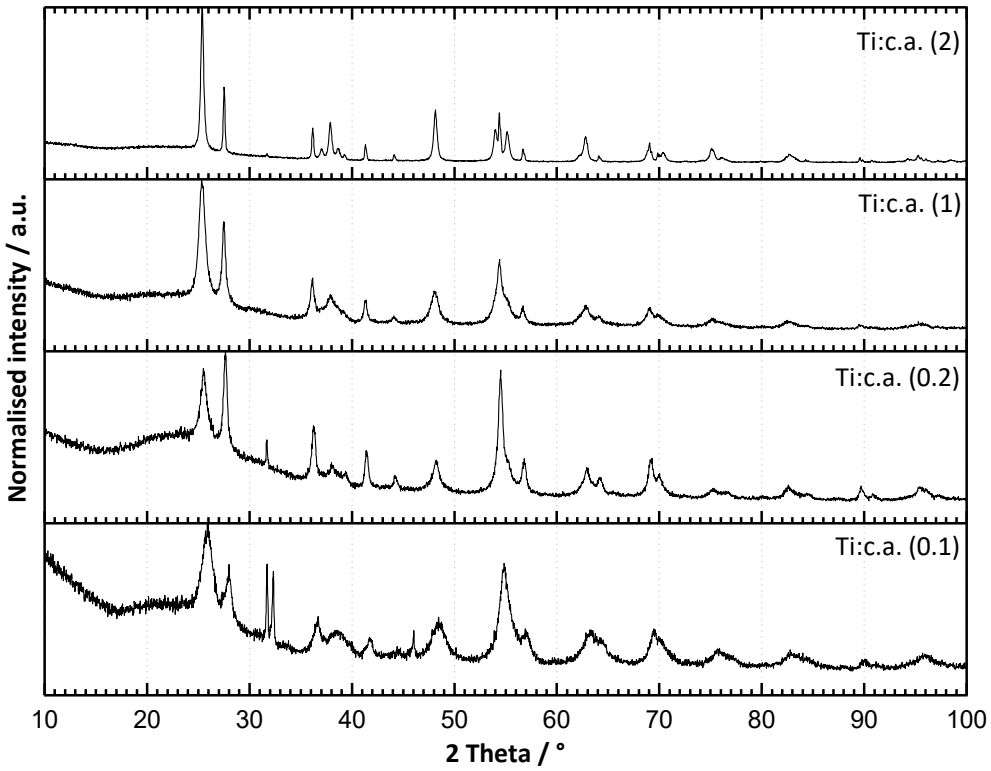

Graph 5.6 Detail of the comparison between diffraction patterns of the TiO_2/C precursor nanocomposite, showing significant peak broadening based on carbon content

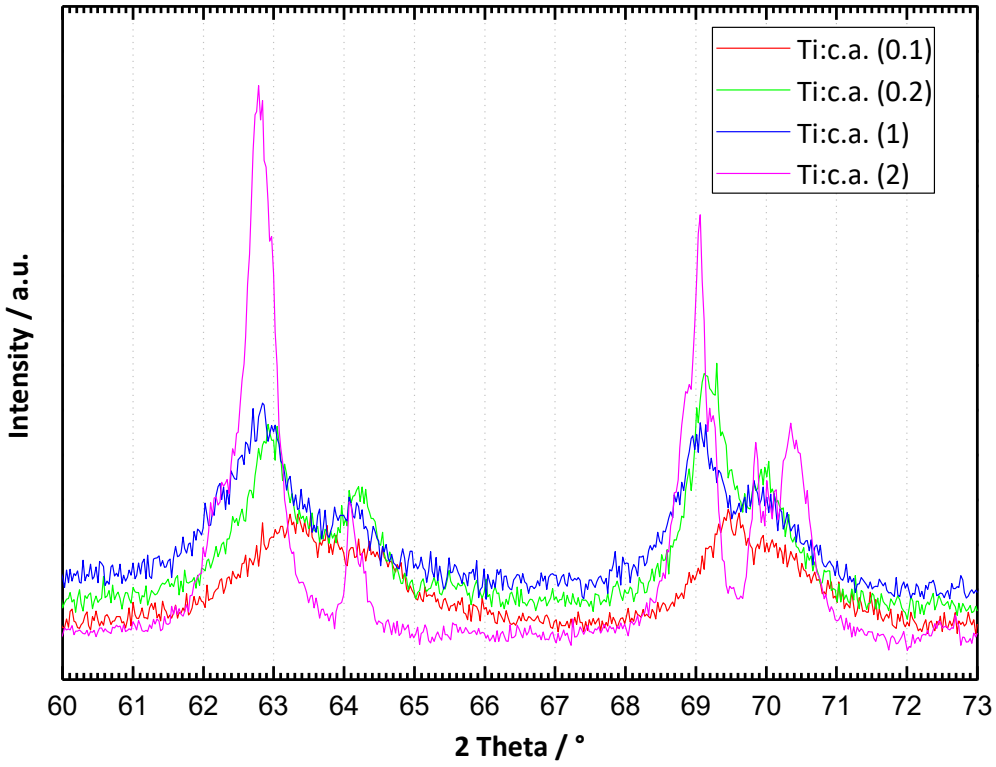

5.1.2 Ti and Al oxide/carbon precursors using chlorides

In the first attempt to prepare Ti_2AlC precursors, the precursors were mixed for the intermediate calcination step in a Ti:Al ratio of 2. Sample 3 was prepared by calcining this mixture of precursors. The PXRD analysis showed no crystalline phase (Graph 5.7). In contrast to sample 2, no diffractions of either anatase or rutile were observed. However, the XRF analysis showed only 8.8 %mol. of aluminium and 89.5 %mol. of titanium (Ti:Al ratio of 10), and the remaining 1.6 %mol. was chlorine residue, most likely due to the low pH of the solution and consequent dimerization and sublimation of $AlCl_3$, which competes with hexahydrate thermal decomposition according to the following equations:

$$2AlCl_3 \cdot 6H_2O \rightarrow Al_2O_3 + 6HCl + 3H_2O$$

$$2AlCl_3 \rightarrow Al_2Cl_6$$

Therefore, a new synthetic approach, described in subsection 4.3.3, was used to minimize the amount of chlorides present in the mixture by using peroxo-titanates instead of HCl-stabilized $TiCl_3$.

Graph 5.7 Diffraction pattern of the $Al_2O_3/TiO_2/C$ precursor nanocomposite (sample 3) – The sample is amorphous.

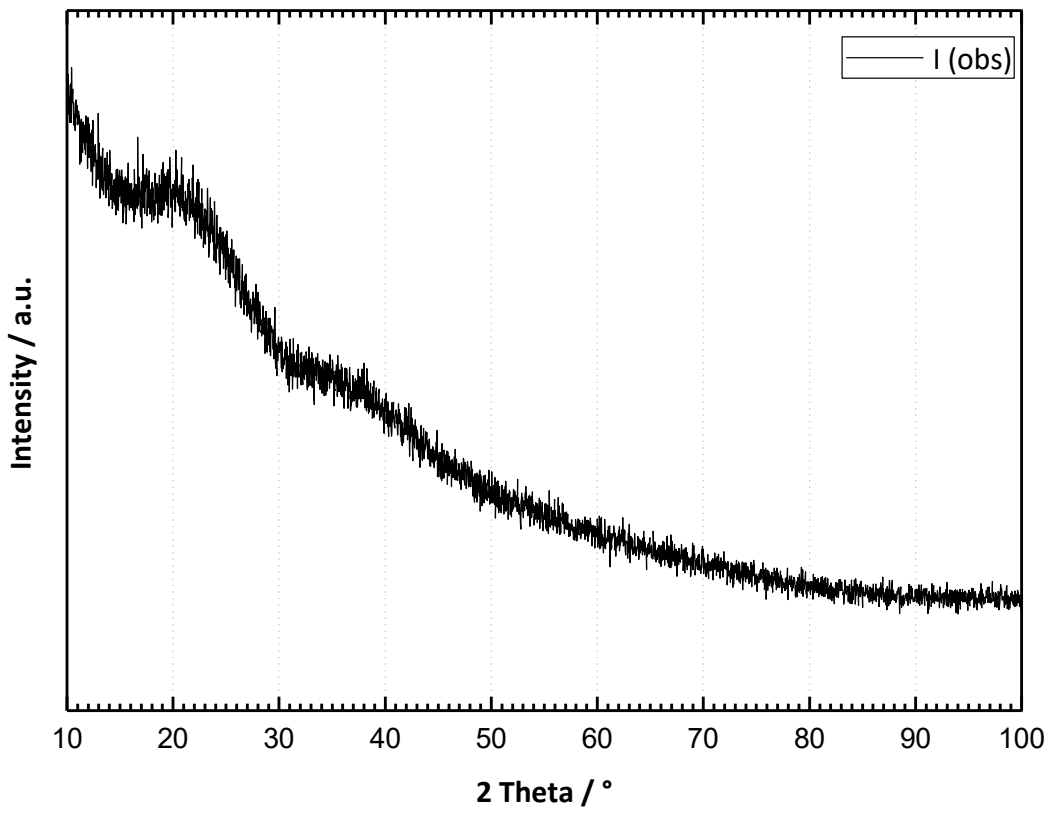

5.1.3 Ti and Al oxide/carbon precursors using peroxo-titanates

In comparison to the binary Al-c.a. system, the ternary Al-Ti-c.a. system exhibited greater aluminium losses. Assuming that the same amount of carbon is formed from the decomposition of citric acid, the expected Ti:Al ratio is approximately 8 (the actual ratio was 10). This shows that adding HCl stabilized $TiCl_3$; thus, the decrease in pH led to further losses of Al.

The synthesis route was adjusted to avoid using chlorides altogether, thereby preventing aluminium chloride sublimation from the solution. This adjustment consisted of using peroxo-titanates, which are synthesized from $TiCl_4$. The chlorides are neutralised by NH_4OH and washed from the solution, as described in subsection 4.3.3. Aluminium nitrate and peroxo-titanic acid (shown in Figure 5.2) were used as sources of alumina and titania, respectively.

Figure 5.2 Peroxo-titanic acid upon synthesis

After one day, some of the H_2O_2 in the PTA solution had decomposed, turning the solution yellow, clouding the solution, increasing the pH and forming a gel sediment over time. Upon shaking, the resulting suspension was stable for more than 1 hour. When $Al(NO_3)_3$ and citric acid were added to the solution, the pH value decreased, and the solution turned orange (shown in Figure 5.3).

Figure 5.3 Left - Clouded PTA; right – clouded PTA after addition of $Al(NO_3)_3$ and citric acid

Two precursor samples were prepared: samples 11 and 12. The Ti:Al:c.a. ratio was 2:1:6 in both cases to assure sufficient carbon content. Sample 11 was calcined as a solution before it evaporated to the point of becoming a gel, whereas sample 12 was evaporated all the way and calcined as a wet gel. The TG-DTA of sample 12 (Graph 5.8) showed 40% weight loss. Assuming all metals remained in the sample in the form of oxides, this corresponds to 6.5 moles of carbon produced from each mole of citric acid. Since that is far in excess of the amount of carbon produced from citric acid, some of the metals must have disappeared.

XRF analysis showed that sample 11 had a Ti:Al ratio of 4.1, which still indicates approximately 50% loss of aluminium. XRF analysis of sample 12 indicated a Ti:Al ratio of 4.3, suggesting a slight decrease in aluminium content. Nevertheless, successfully more aluminium remained in the mixture when using PTA than when using chlorides. This difference in aluminium loss is approximately 40%. Some Al losses are expected in MAX Phase synthesis [37]–[39] as a result of the low aluminium melting point (660 °C). Assuming that some of the precursor undergoes reduction in the step of precursor synthesis, some of the aluminium will be lost in this step as well. Moreover, aluminium loss was also observed in the binary Al:c.a. system (see subsection 5.1.1). This method was therefore used to synthesize the precursors of the Ti_2AlC MAX phase.

PXRD analysis of sample 12 (Graph 5.9) showed one crystalline phase (rutile) with an average apparent crystallite size of 10.7 nm, in line with the binary Al-c.a. and Ti-c.a. systems, where only the TiO_2 crystalline phase developed.

SEM shows particle sizes of up to 50 micrometres (Figure 5.4). The particle surface with open pores is shown in detail in Figure 5.5. The SEM-EDS (Figure 5.6) map shows that the sample contains small particles of homogeneous oxide mixtures along with larger particles of carbon.

This is further supported by the TEM images (Figure 5.7, detail in Figure 5.8), which show particles of approximately 10-20 nanometres of oxides embedded in the carbon matrix. The particle sizes observed in SEM correspond to these matrices containing small oxide particles. The sizes of the oxide particles, as determined by TEM, corroborate the PXRD data.

Graph 5.8 TG-DTA of TiO_2/Al_2O_3/C precursor nanocomposite sample 12

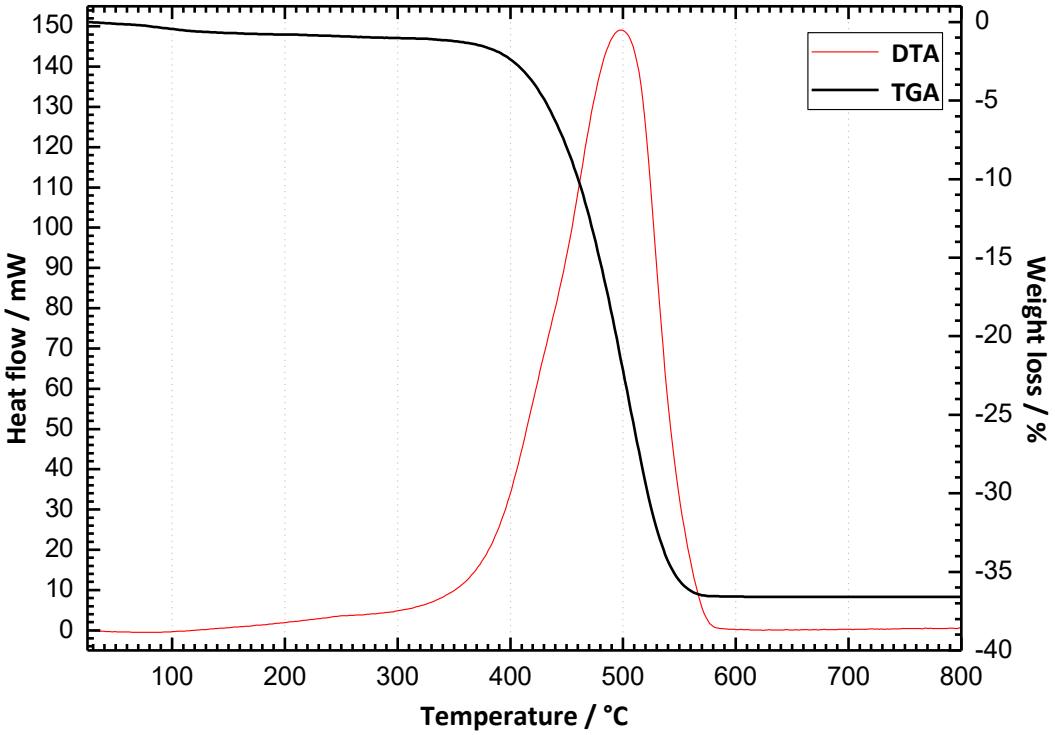

Graph 5.9 Diffraction pattern of TiO_2/Al_2O_3/C precursor nanocomposite (sample 12) – only one crystalline phase (rutile)

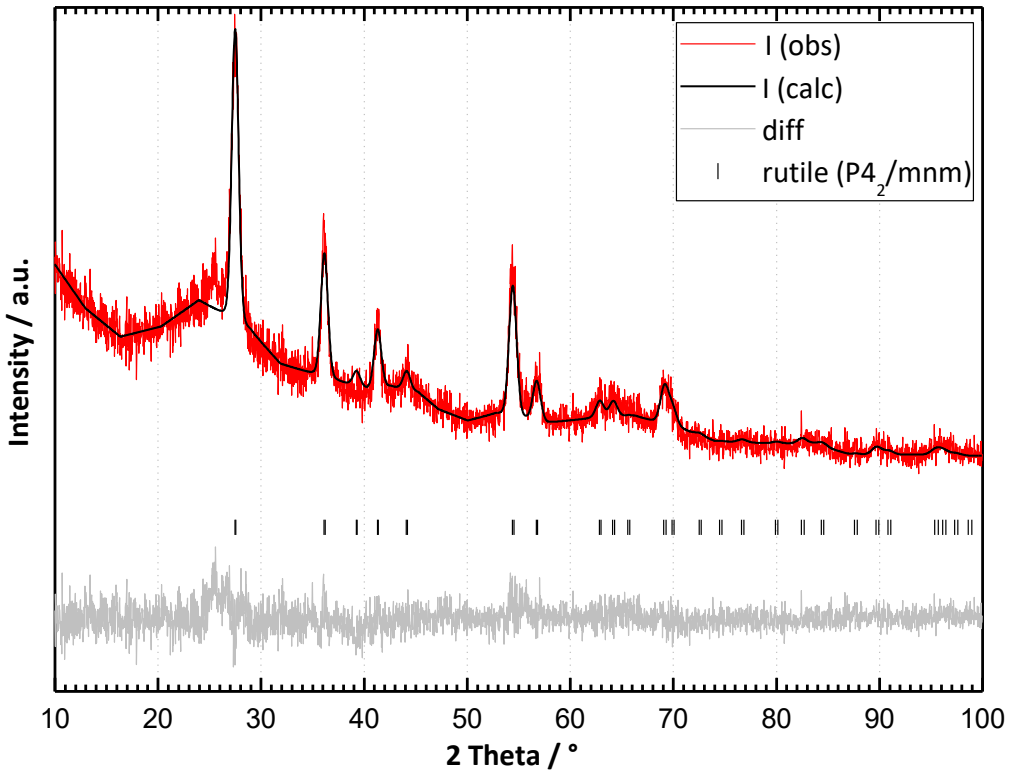

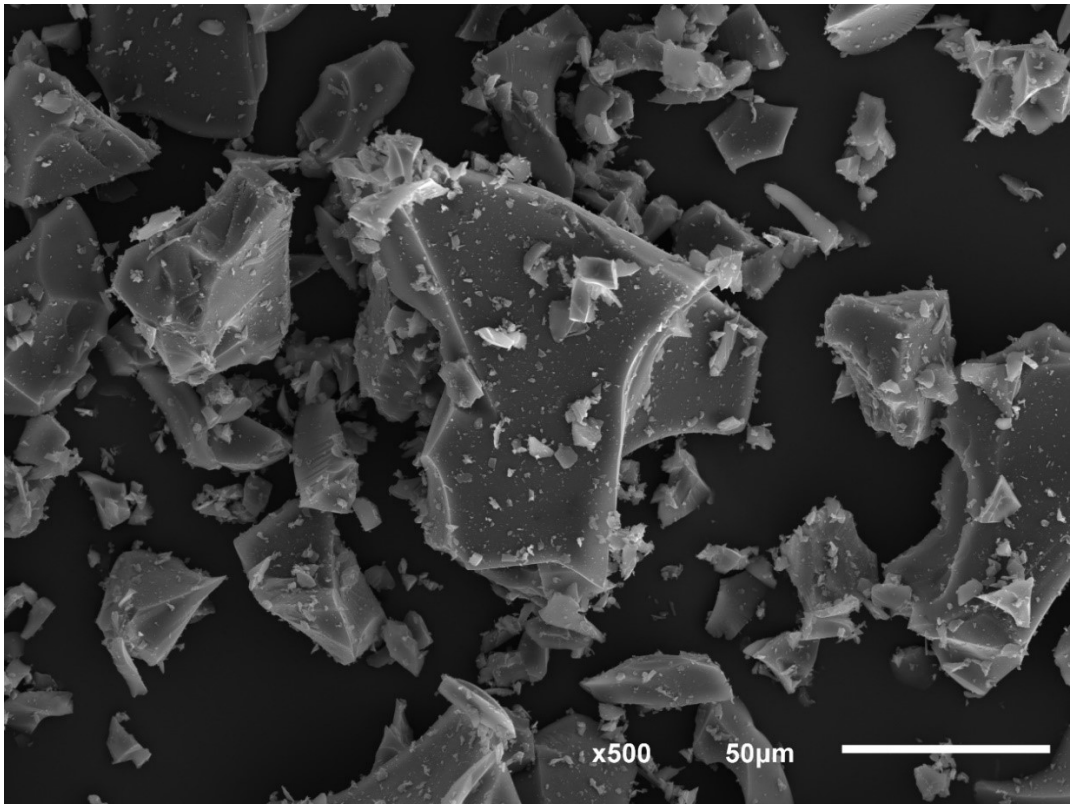

Figure 5.4 SEM of $TiO_2/Al_2O_3/C$ precursor nanocomposite (sample 12) - secondary electrons (500x magnification)

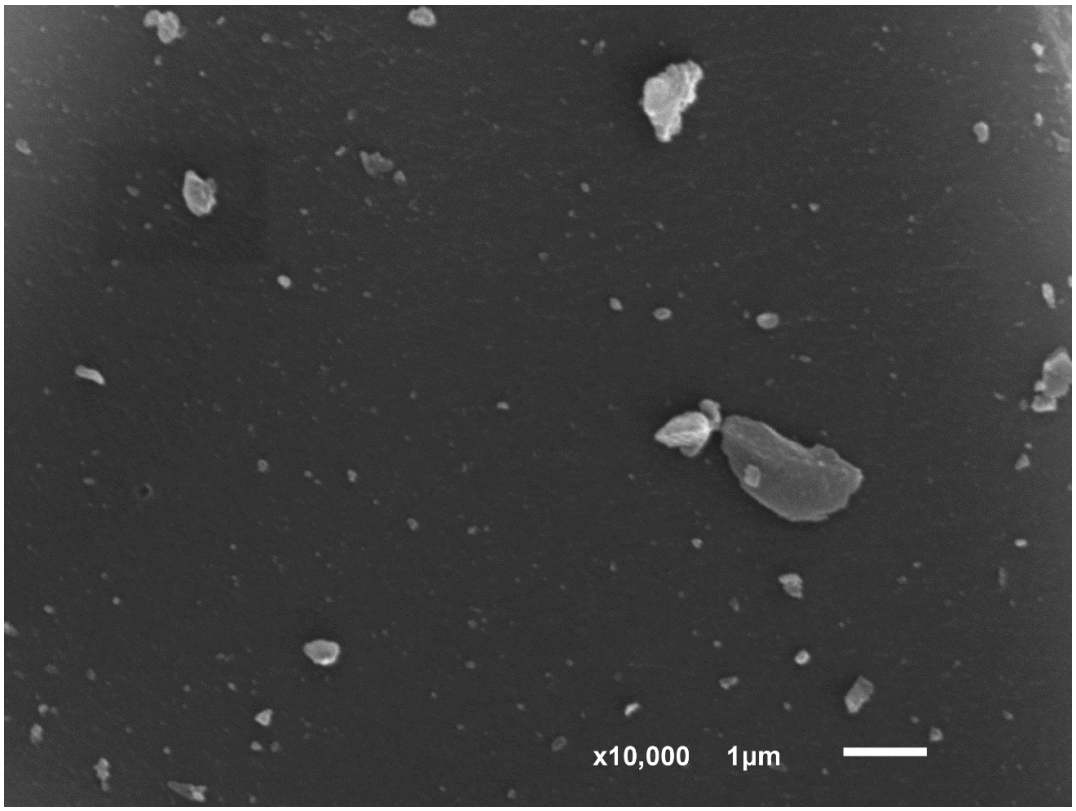

Figure 5.5 SEM of $TiO_2/Al_2O_3/C$ precursor nanocomposite (sample 12) - secondary electrons (10,000x magnification)

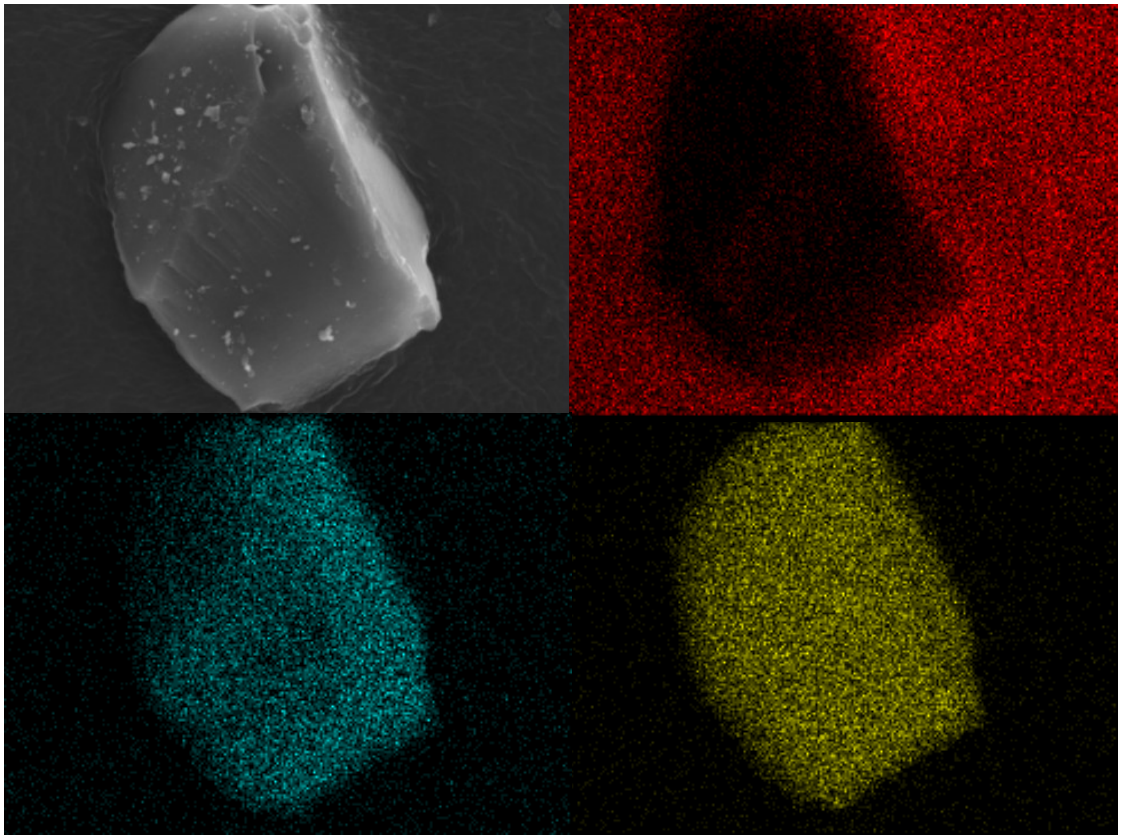

Figure 5.6 SEM-EDS - element maps of $TiO_2/Al_2O_3/C$ precursor nanocomposite (sample 12) top left – electron image, red – carbon, blue – aluminium, yellow – titanium

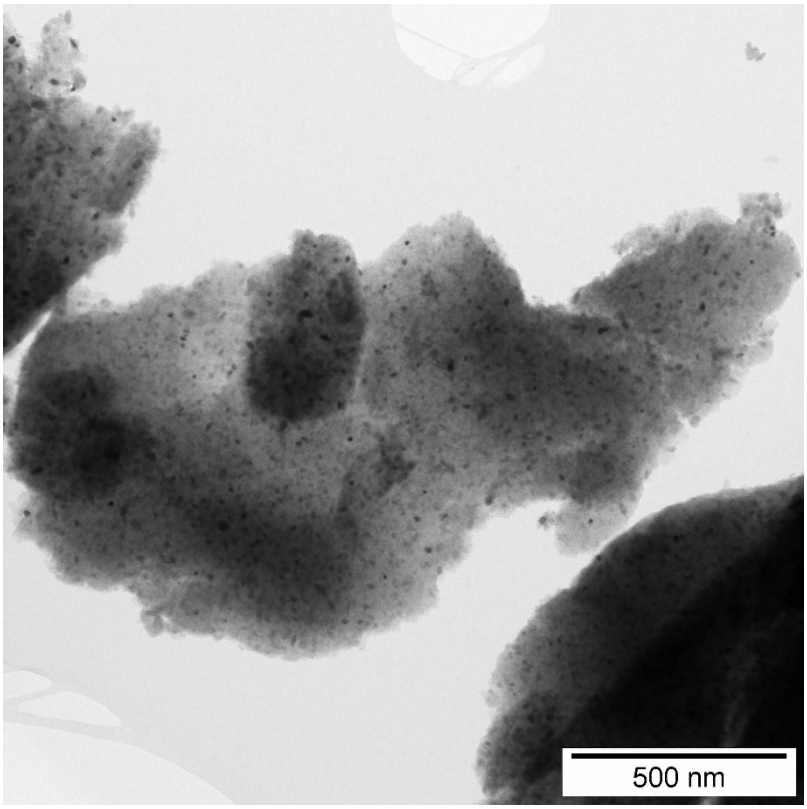

Figure 5.7 TEM image of $TiO_2/Al_2O_3/C$ precursor nanocomposite (sample 12) - carbon matrix with embedded oxide nanoparticles

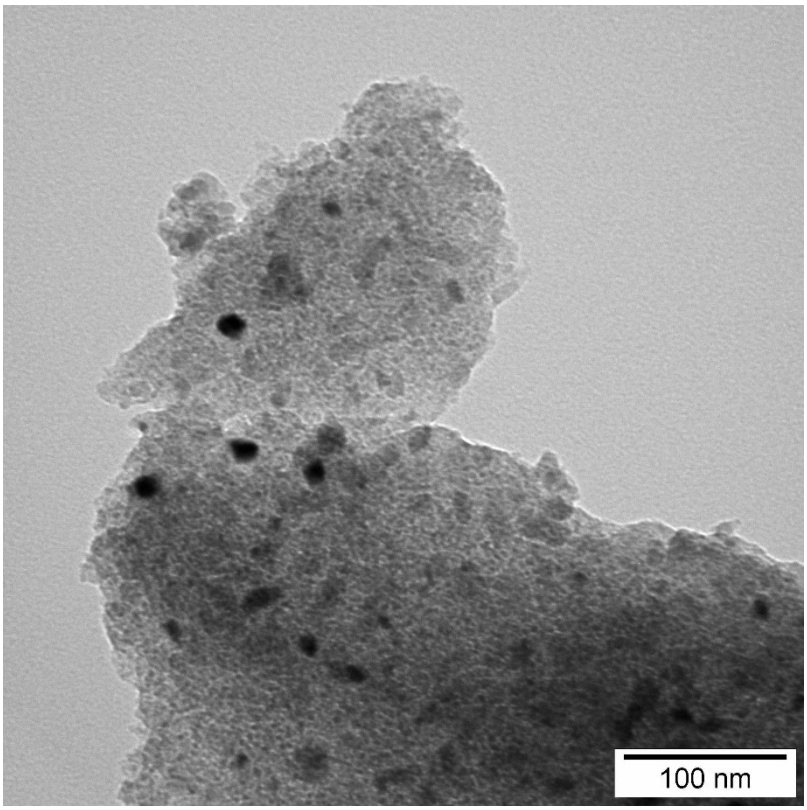

Figure 5.8 TEM - detail of $TiO_2/Al_2O_3/C$ precursor nanocomposite (sample 12) – carbon matrix with embedded oxide nanoparticles

5.2 Products of SPS treatment

The oxidic precursors were consequently used to synthesize carbides in the SPS machine. Except for sample 14, which was synthesized in argon atmosphere, the reactions were observed indirectly through pressure changes in the SPS chamber, as outlined in Graph 5.10. The first maximum in pressure (approximately 50. – 200. sec.) is caused by desorption of gases from both the sample and graphite parts of the apparatus. The second maximum (approximately 200. – 400. sec.) is caused by gases evolving from the carbothermal reduction. The samples were heated at a heating rate of 200 °C/min and the temperatures were maintained for 20 minutes. The delay in actual temperature at the beginning of the cycle is caused by the pyrometer, which operates from 500 °C.

Graph 5.10 Heating cycle used for SPS carbide synthesis –
comparison of pressure with blank - no sample (yellow) and with oxide-carbon precursor mixture (grey)
red – set temperature, blue – actual temperature

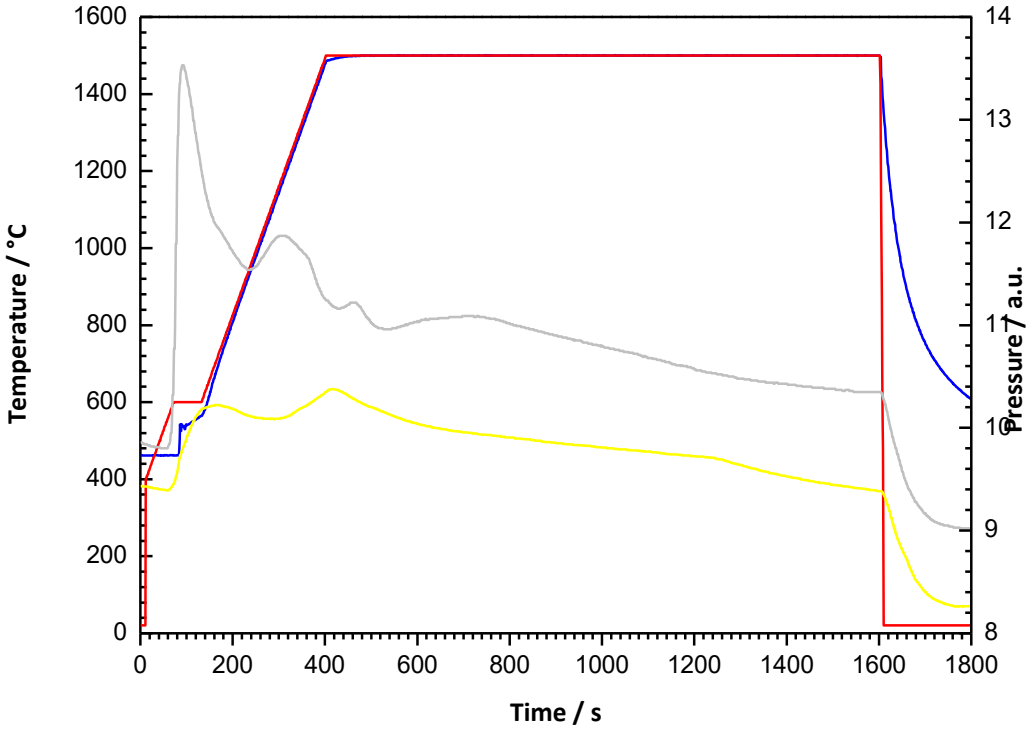

5.2.1 Single metal carbides

Aluminium carbide and titanium carbide were synthesized from alumina/titania and carbon resulting in yellow and black powders, respectively (shown in Figure 5.9).

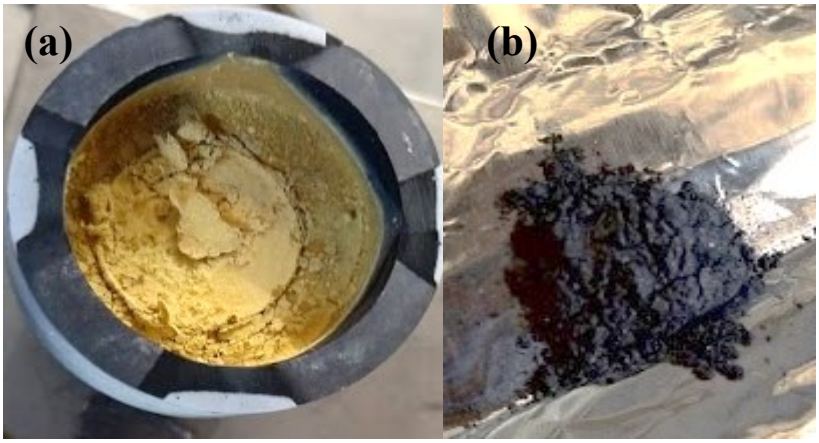

Figure 5.9 (a) Al_4C_3 in a graphite punch; (b) TiC

The first batch of Al_4C_3 samples (5 - 8), with Al:c.a. ratios ranging from 1 to 0.5, was prepared from the precursors obtained by the first imperfect heating cycle. Therefore, the Al:c.a. ratios in the mixtures are proportional to the Al:C ratios after calcining, as shown by the presence of unreacted, crystalline Al_2O_3 for some c.a. contents, but not others. The comparison of diffraction patterns is shown in Graph 5.13, which highlights that aluminium carbide was formed in each case, albeit in different amounts. Sample 5, with an Al:c.a. ratio of 1, resulted in complete conversion to Al_4C_3 after 20 minutes of SPS treatment at 1500 °C (Graph 5.11), whereas sample 8, with an Al:c.a. ratio of 0.5, still contained 69.3% of Al_2O_3, which accounts for 61.4 % of the aluminium present in the sample, based on the Rietveld analysis (Graph 5.12).

The average apparent sizes of Al_4C_3 crystallites ranged from 54.6 to 78.2 nm, regardless of carbon content. All later syntheses were conducted using the new heating cycle, which resulted in consistent carbon amounts in the precursor. PXRD analysis of these early samples also showed sample contamination with graphite (graphite peak at 26° in Graph 5.11, Graph 5.12 and Graph 5.13) derived from the graphite foil used during the synthesis. For this reason, graphite foil was replaced by tungsten foil in subsequent experiments.

The SEM of sample 5 showed very fine particles (Figure 5.10 and Figure 5.11) without distinct morphology features. The sample remained an unsintered powder. This lack of sintering may be caused by the high melting point of Al_2O_3, which hampers the diffusion rates.

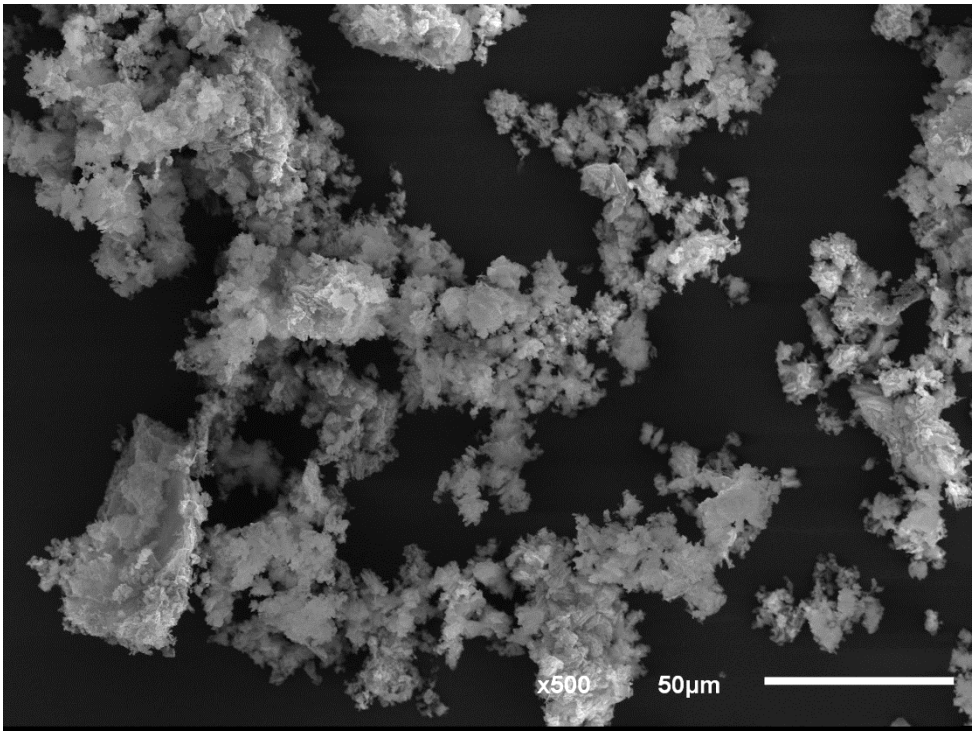

Figure 5.10 SEM of Al_4C_3 (sample 5) - secondary electrons (500x magnification)

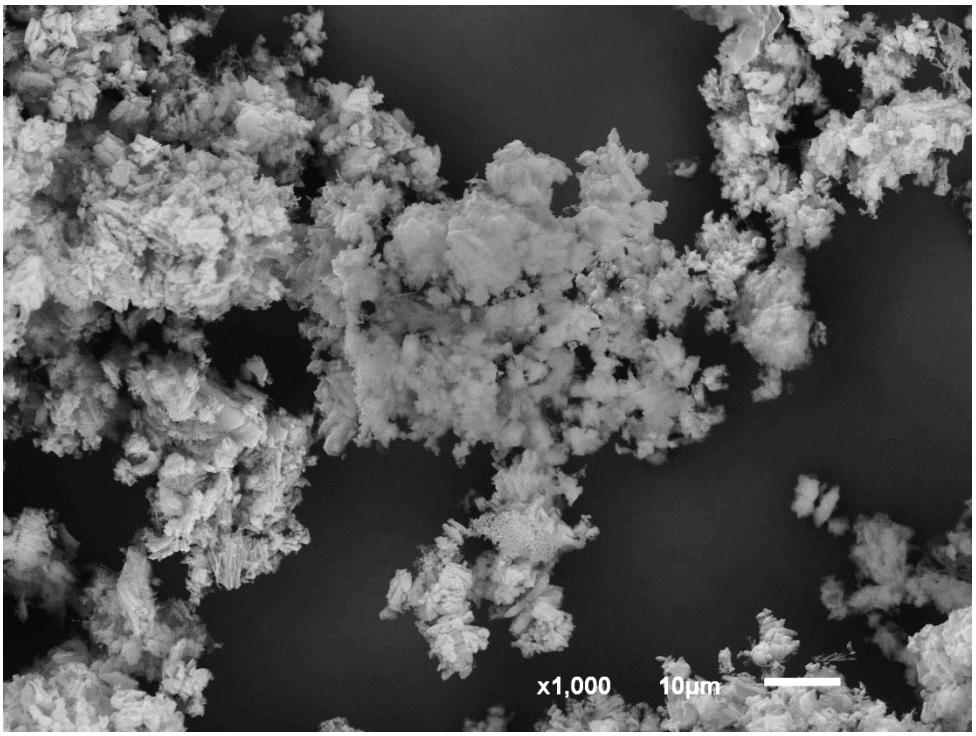

Figure 5.11 SEM of Al_4C_3 (sample 5) - secondary electrons (1,000x magnification)

Graph 5.11 Diffraction pattern of Al_4C_3 (sample 5) – nanocomposite of Al_2O_3 and C treated at 1500 °C The diffraction at 26° belongs to the graphite from used graphite foil

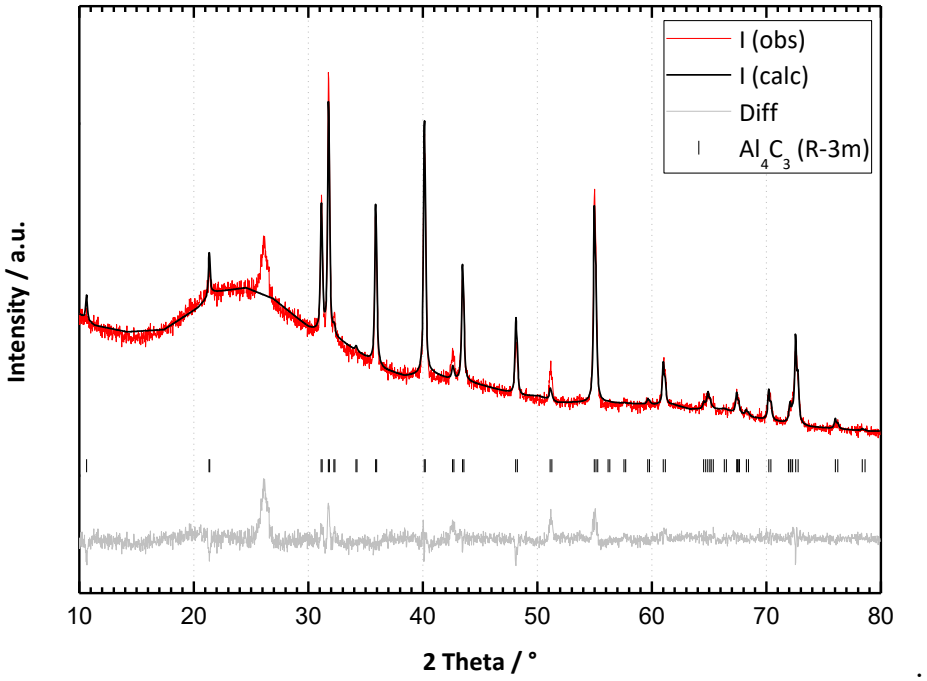

Graph 5.12 Diffraction pattern of Al_4C_3/Al_2O_3 mixture (sample 8) – composite of Al_2O_3 and C treated at 1500 °C. The diffraction at 26° belongs to the graphite from used graphite foil

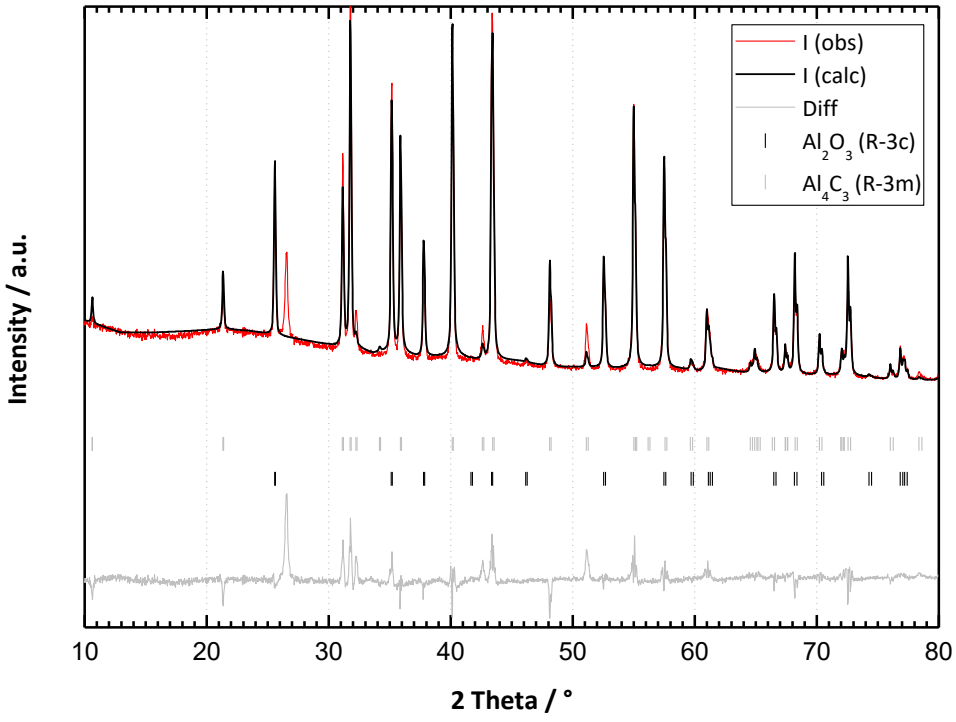

Graph 5.13 Diffraction patterns of Al_4C_3 (samples 5 – 8) – composites of Al_2O_3 and C treated at 1500 °C. Some of the diffraction lines of unreacted Al_2O_3 are shown between the red dashed lines

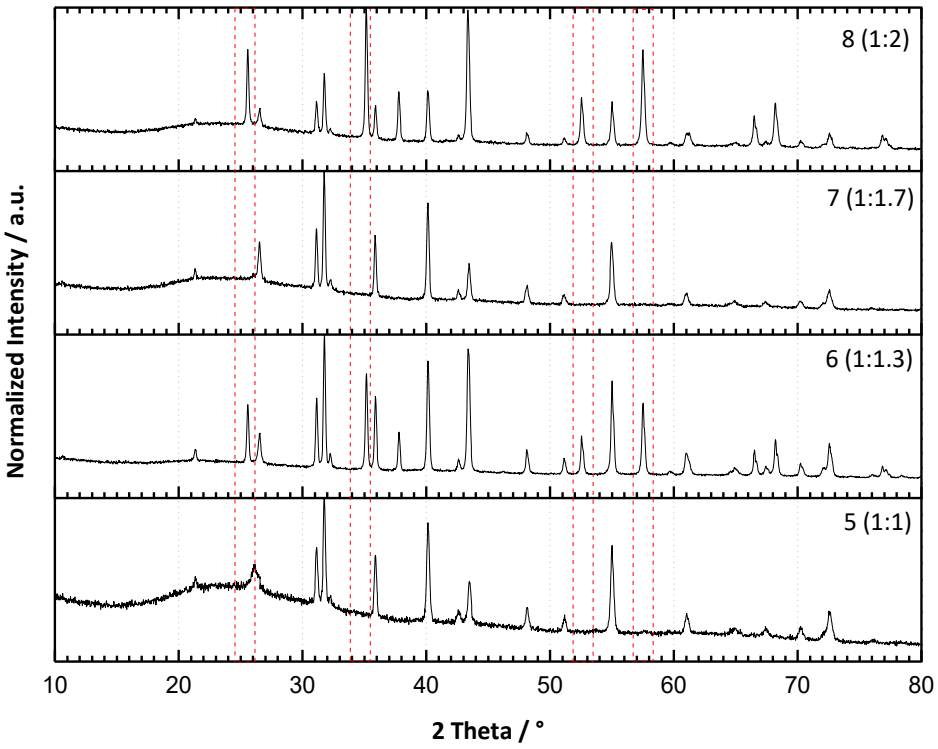

The TiC samples were prepared with Ti:c.a. ratios ranging from 1 to 0.5. All samples displayed full conversion after 20 minutes of SPS treatment at 1500 °C. The diffraction pattern of sample 9 (Ti:c.a. ratio 1) is shown in Graph 5.14. This pattern contains single-phase TiC with sharp peaks. The average apparent crystallite size, according to the Scherrer formula, is 107 nm.

Sample 9 shows larger particles than sample 5 based on SEM. The particles are partly sintered into chunks of up to 50 micrometres (Figure 5.12). The detail (Figure 5.13) shows primary grains up to approximately one micrometre in size.

Two phenomena mat explain why these particles (sample 9) are larger than Al_4C_3 (sample 5):

1) higher diffusion rate of Ti ions

2) decrease in the aluminium content of the Al_4C_3 precursor and subsequent diffusion barrier caused by the excess carbon

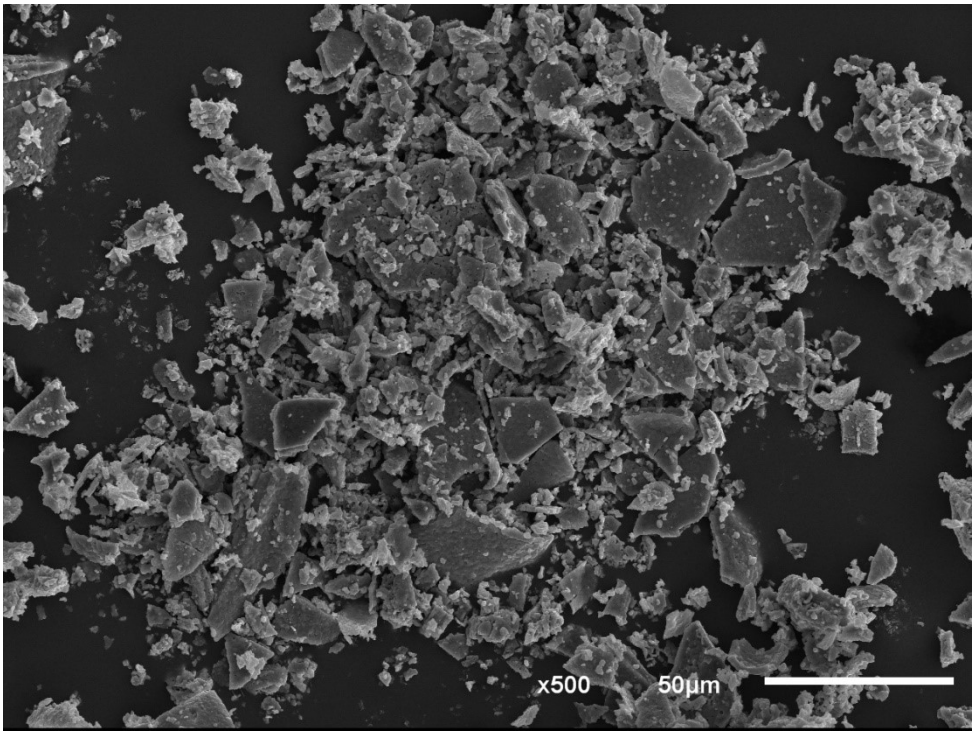

Figure 5.12 SEM of TiC (sample 9) - secondary electrons (500x magnification)

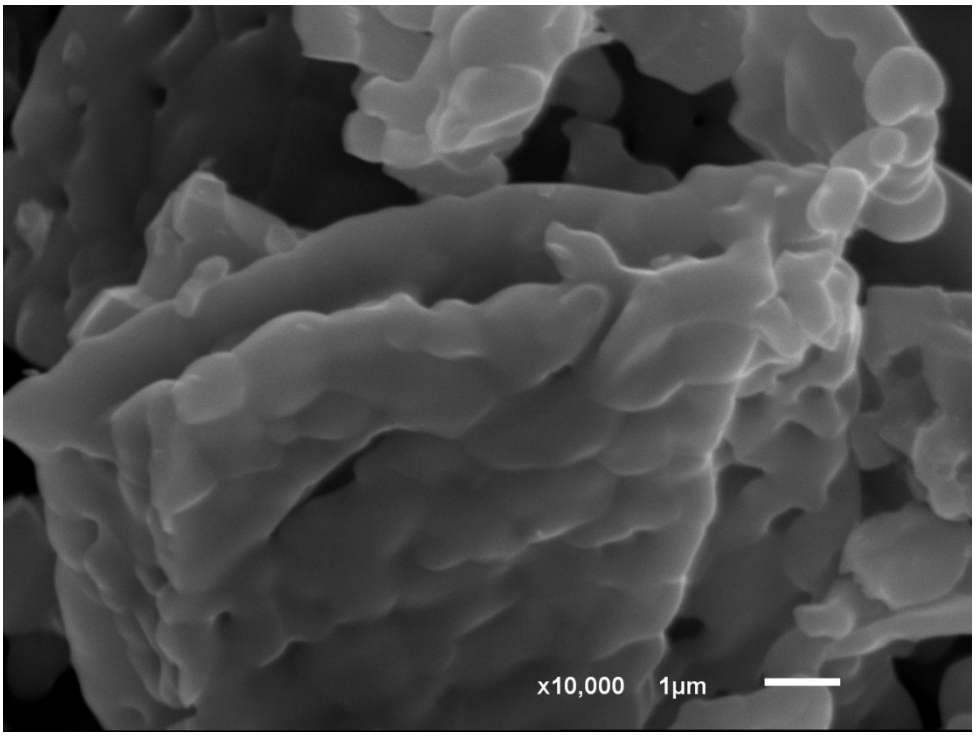

Figure 5.13 SEM detail of TiC (sample 9) - secondary electrons (10,000x magnification) showing primary particles (~500 nm) sintered together

Graph 5.14 Diffraction pattern of TiC (sample 9) – composite of TiO_2 and C treated at 1500 °C

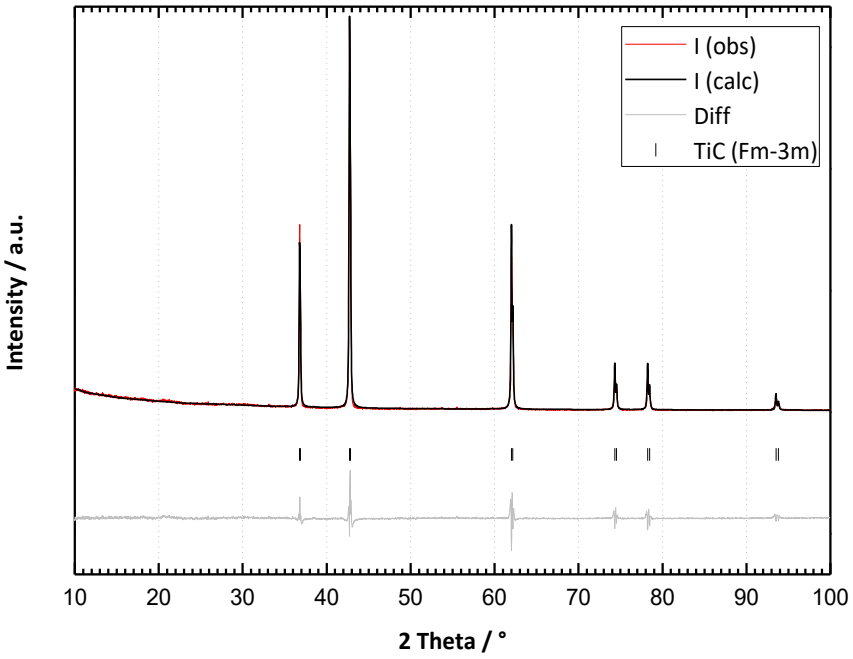

5.2.2 Mixed metals carbides

Preparing Ti_2AlC was a difficult task. Although titanium and aluminium chlorides were initially used, PXRD analysis of sample 10 (Graph 5.15) showed that the only crystalline phase after 20 minutes of SPS treatment at 1500 °C was titanium carbide.

In addition, XRF analysis showed that either no aluminium was present in the final product or its amount was smaller than the detection limit of the method. The possible absence of aluminium can be partly explained by the disappearance of Al in the Al-c.a. binary system, which lost some of its aluminium content itself. Adding HCl-stabilized $TiCl_3$ decreases the pH, thus increasing the $AlCl_3$ dimerization due to its absence in the oxidic precursors, which were subsequently analysed by XRF as well (described in subsection 5.1.2).

Furthermore, SEM showed that the sample was chemically homogeneous, thus demonstrating the disappearance of aluminium, as also shown by BSE imaging (contrast with chemical composition), image which displays that all of the sample with approximately the same brightness (Figure 5.16). The SEM showed powder with grains up to 50 micrometres (Figure 5.14 and Figure 5.15). The morphology and particle size are similar to those of the Ti-c.a. system and therefore different from those of the Al-c.a. system, as described in subsection 5.2.1 above.

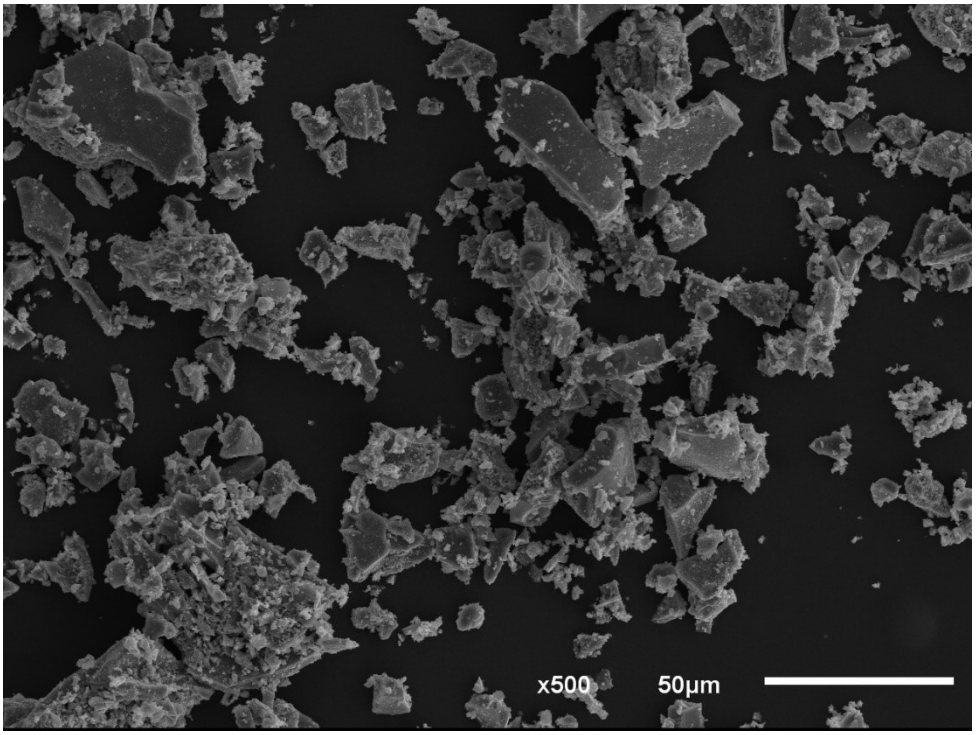

Figure 5.14 SEM of TiC (sample 10) – chloride precursors treated at 1500 °C - secondary electrons (500x magnification)

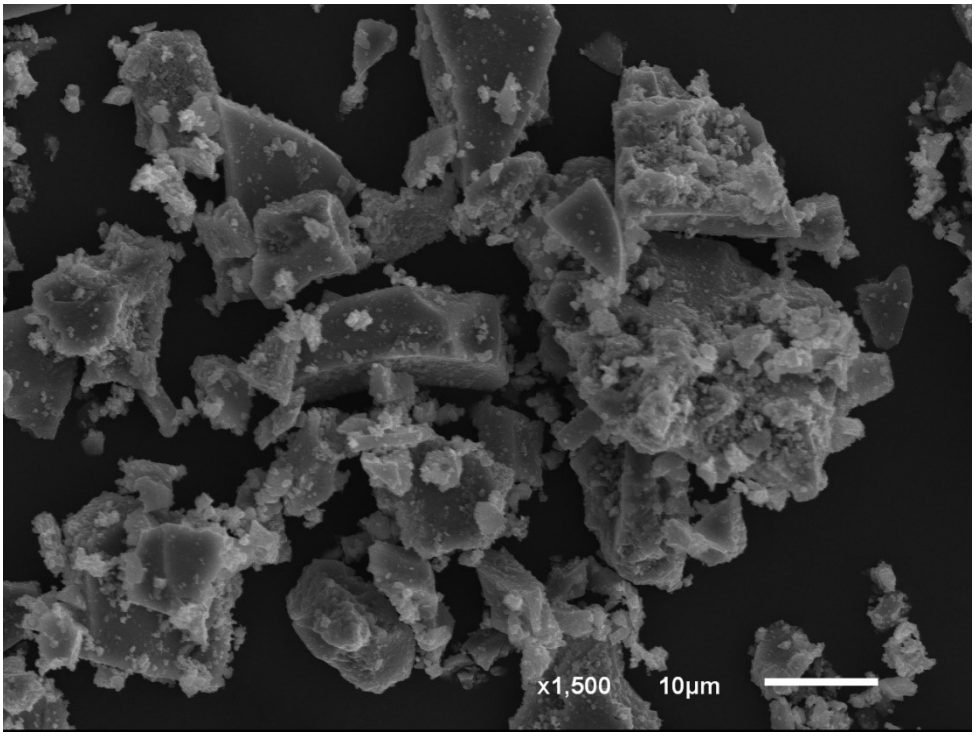

Figure 5.15 SEM of TiC (sample 10) – chloride precursors treated at 1500 °C - secondary electrons (1,500x magnification)

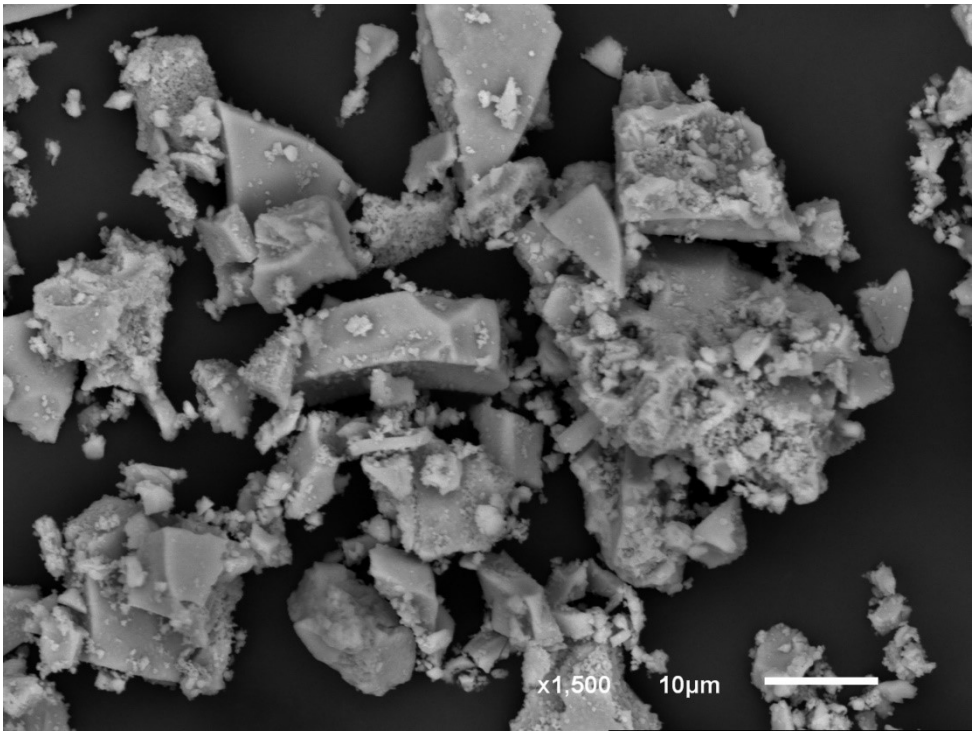

Figure 5.16 SEM of TiC (sample 10) – chloride precursors treated at 1500 °C - back-scattered electrons (1,500x magnification)

Graph 5.15 Diffraction pattern of TiC – chloride precursors treated at 1500 °C (sample 10) After synthesis, the only observable phase is TiC, with no Al-based phases present in the sample

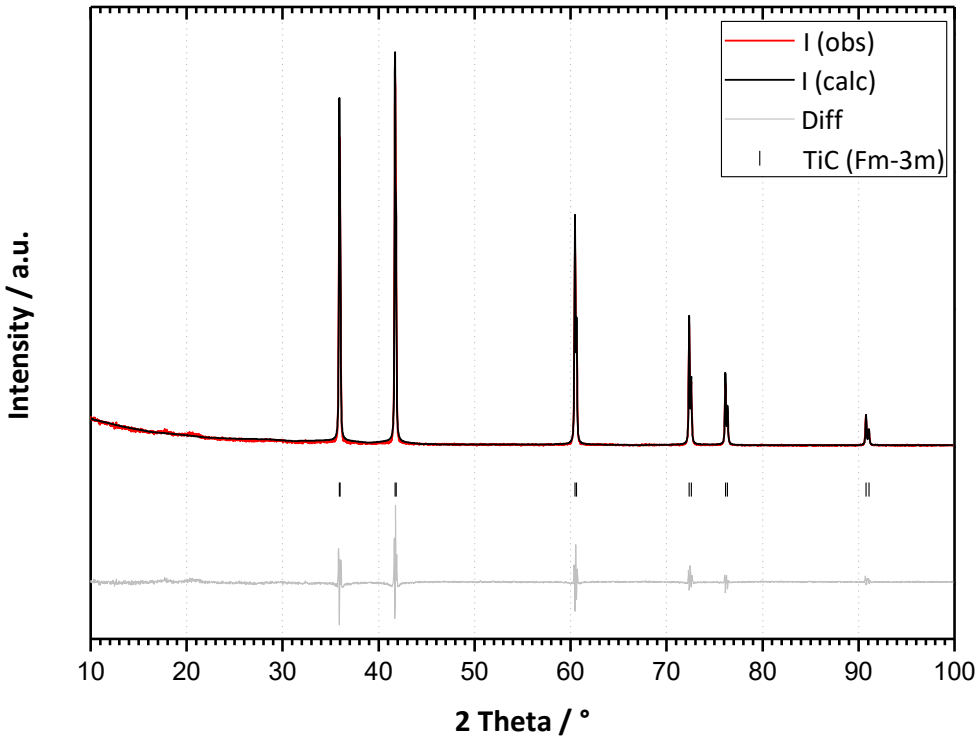

Aluminium was present in the intermediate product after implementing the new synthetic method, as shown by XRF analysis (subsection 5.1.3). When both Ti and Al were present, the reaction yielded different compounds, depending on the experimental conditions, as outlined in Table 5.1.

Table 5.1 Conditions and results of mixed-metal carbide synthesis

Sample	Temperature [°C]	pressure	Phases
13	1400	vacuum	TiC + Al_4C_3
14	1400	1 atm Ar	TiC + Al_2O_3
15	1100	vacuum	TiC
16	1200	vacuum	TiC
17	1300	vacuum	TiC
18	1400	vacuum	TiC + Al_4C_3

Samples 13 and 14 were synthesized from the same precursor batch, sample 11 (subsection 5.1.3). The purpose of those samples was to determine whether vacuum or argon atmosphere was more suitable for the synthesis. While sample 13 (Graph 5.16) contained Al_4C_3, sample 14 (Graph 5.17) only contained Al_2O_3 along with TiC, as shown by PXRD. Sample 13 contained 10.8 % of Al_4C_3 (with an average apparent size of 16 nm), as shown by Rietveld analysis. These data correspond to a Ti:Al molar ratio of 5. In turn, sample 14 contained 16.2 % of Al_2O_3 (average apparent size 58 nm), which corresponds to a Ti:Al molar ratio of 4.4. The results show decreases in relative aluminium content of 16 and 7.4 %, respectively, corroborating the losses reported by other researchers [37]–[39]. The average apparent sizes of TiC crystallites were 11.7 nm for sample 13 and 13.0 nm for sample 14.

The presence of Al_4C_3 phase in sample 13 indicates that removing the gaseous side-products by continuous evacuation of the reaction chamber shifts the equilibrium in favour of the carbide products.

XRF, however, showed slightly different numbers: the Ti:Al ratios were 7.2 for sample 13 (45% loss of Al) and 2.9 for sample 14 (28.3% loss of Ti). Thus, the crystallinity of some products may not be high enough for detection by PXRD. This hypothesis is supported by the fact that Al_2O_3 has a higher melting point than TiO_2 and therefore a higher temperature required for diffusion. In conclusion, the available data and the standardless method used for XRF do not enable us to assess whether all precursors reacted. Table 5.2 shows the comparison between XRF and PXRD analyses.

The SEM of sample 13 (Figure 5.17 and Figure 5.18) showed grains of up to 50 micrometres. In detail (Figure 5.19), a surface with open porosity and fine nanoparticles is highlighted.

The SEM of sample 14 (Figure 5.20, Figure 5.21 and Figure 5.22) shows similar morphology to that of sample 13, most likely due to the composition of both samples, which mostly consist of carbon and TiC, with only small portions of the respective Al-Phases.

Table 5.2 Ti:Al ratios of samples 11 – 18. Comparison of PXRD and XRF where applicable.

Precursor			**Product**			
Sample	Initial ratio	after calcining	Sample	XRF	PXRD	Phases
11	1.8	4.1 (XRF)	13	7.2	5.0	$TiC+Al_4C_3$
			14	2.9	4.4	$TiC+Al_2O_3$
12	1.8	4.3 (XRF)	15	3.7	-	TiC
			16	3.7	-	TiC
			17	3.8	-	TiC
			18	3.9	26.7	$TiC+Al_4C_3$

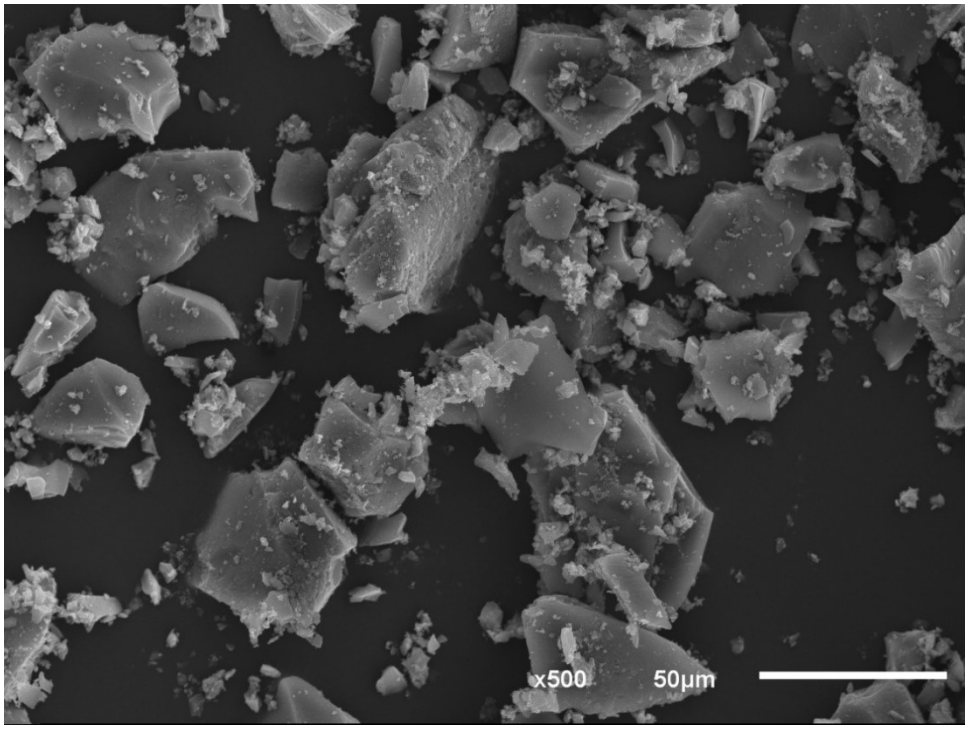

Figure 5.17 SEM of TiC/Al_4C_3 composite (sample 13) - secondary electrons (500x magnification)

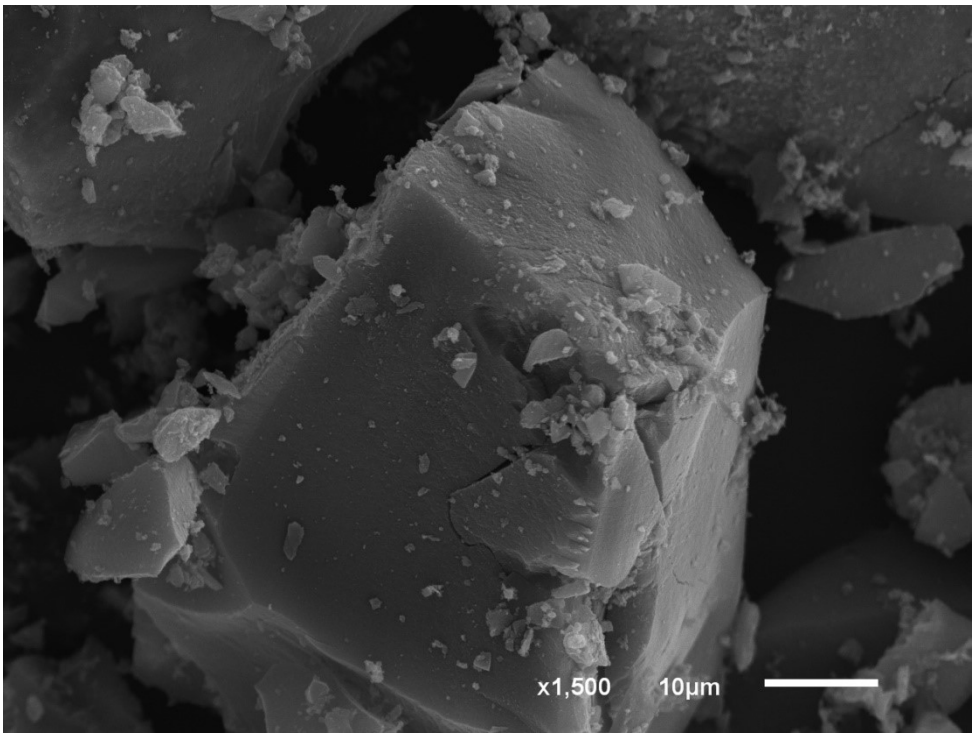

Figure 5.18 SEM of TiC/Al_4C_3 composite (sample 13) - secondary electrons, detail of a grain (1,500x magnification)

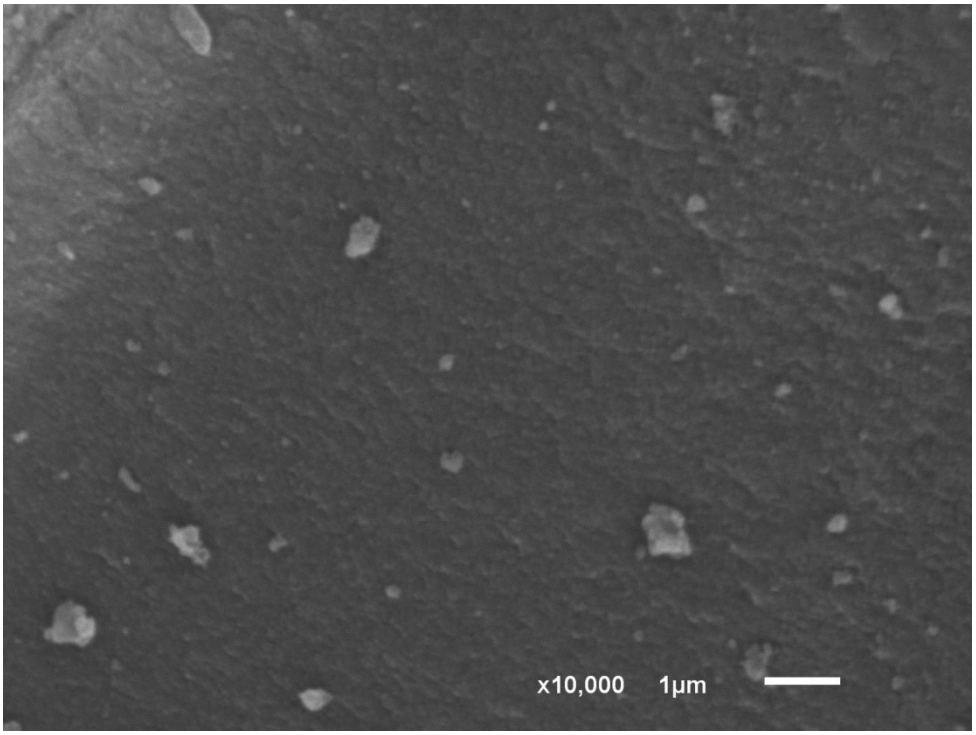

Figure 5.19 SEM of TiC/Al_4C_3 composite (sample 13) – secondary electrons, detail of grain surface (10,000x magnification)

Graph 5.16 Diffraction pattern of $TiC\text{-}Al_4C_3$ mixture (sample 13) – obtained by treating the $Al_2O_3/TiO_2/C$ nanocomposite at 1400 °C in vacuum

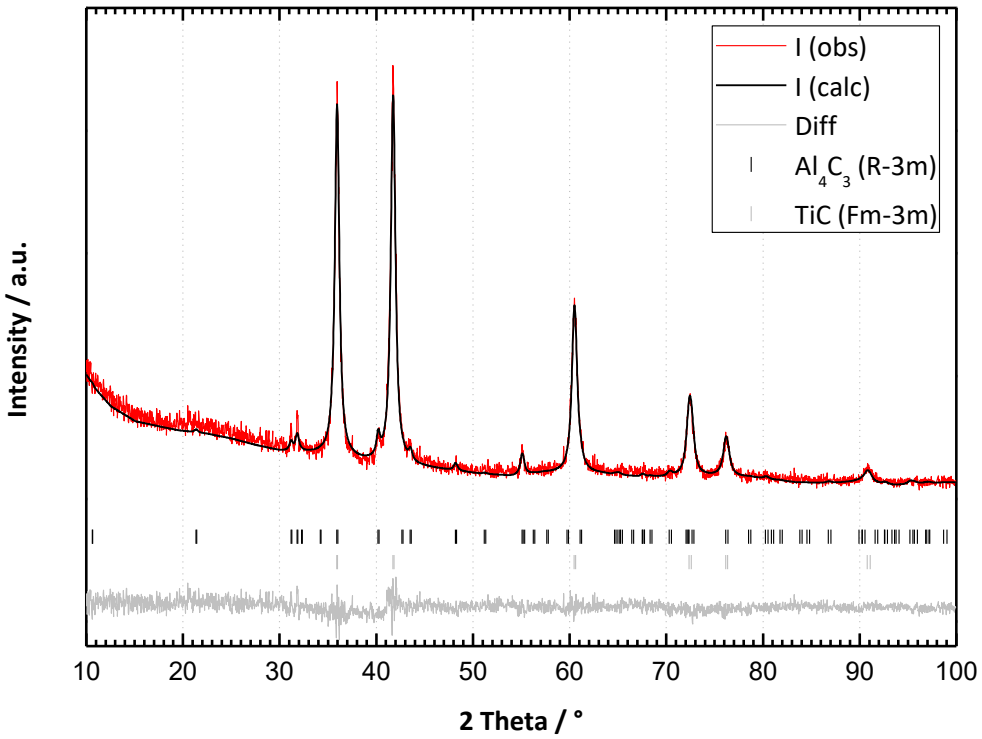

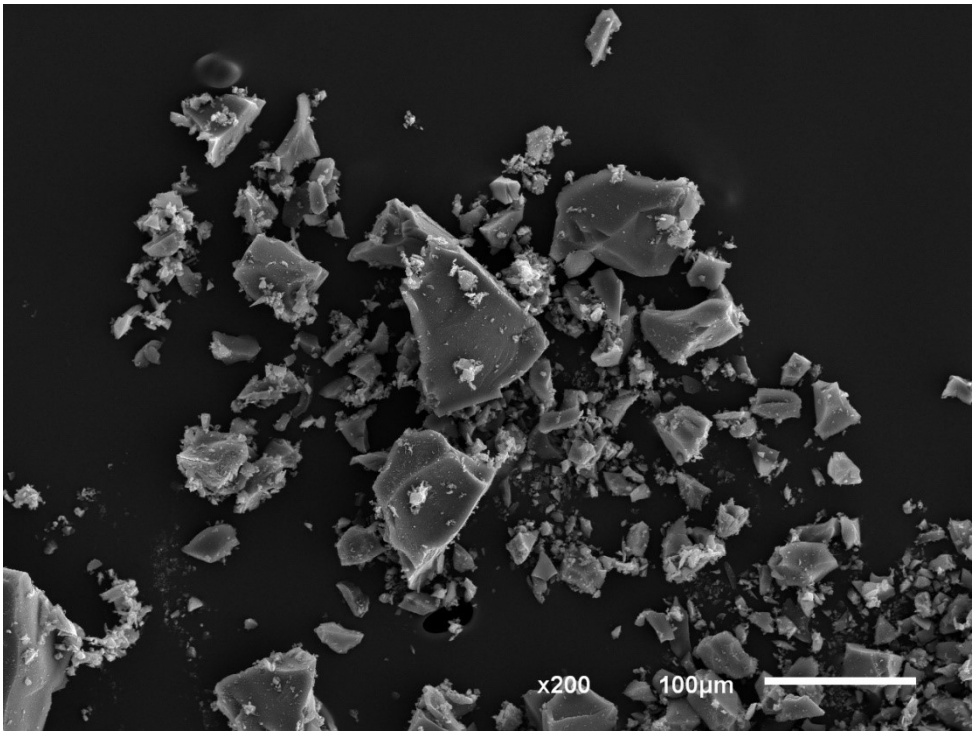

Figure 5.20 SEM of TiC/Al_2O_3 composite (sample 14) - secondary electrons (200x magnification)

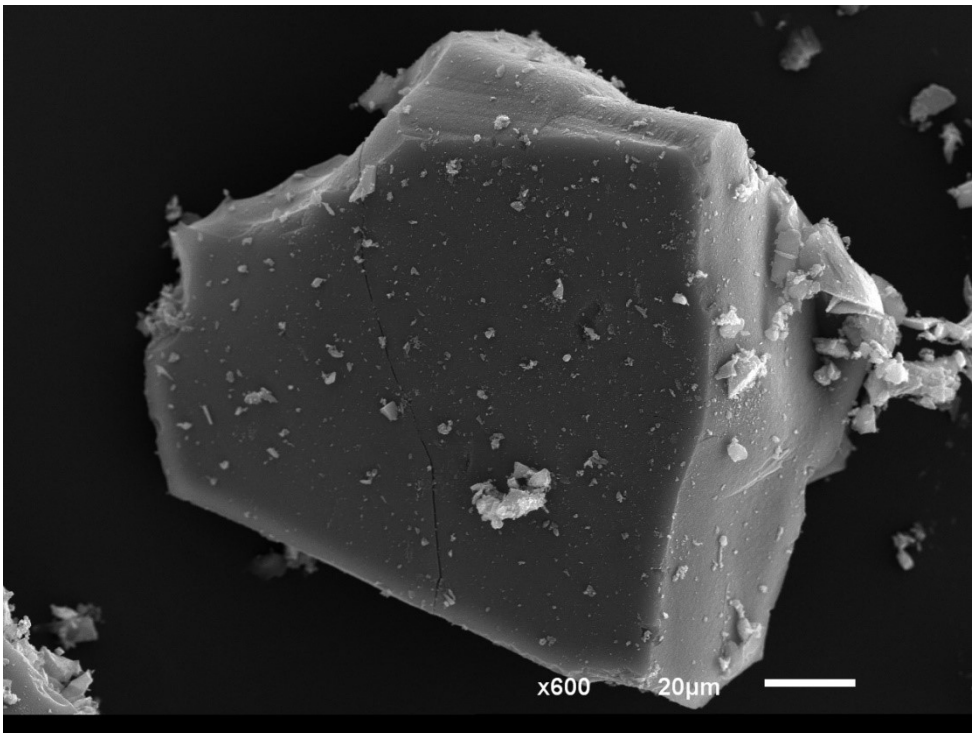

Figure 5.21 SEM of TiC/Al_2O_3 composite (sample 14)- secondary electrons, detail of a grain (600x magnification)

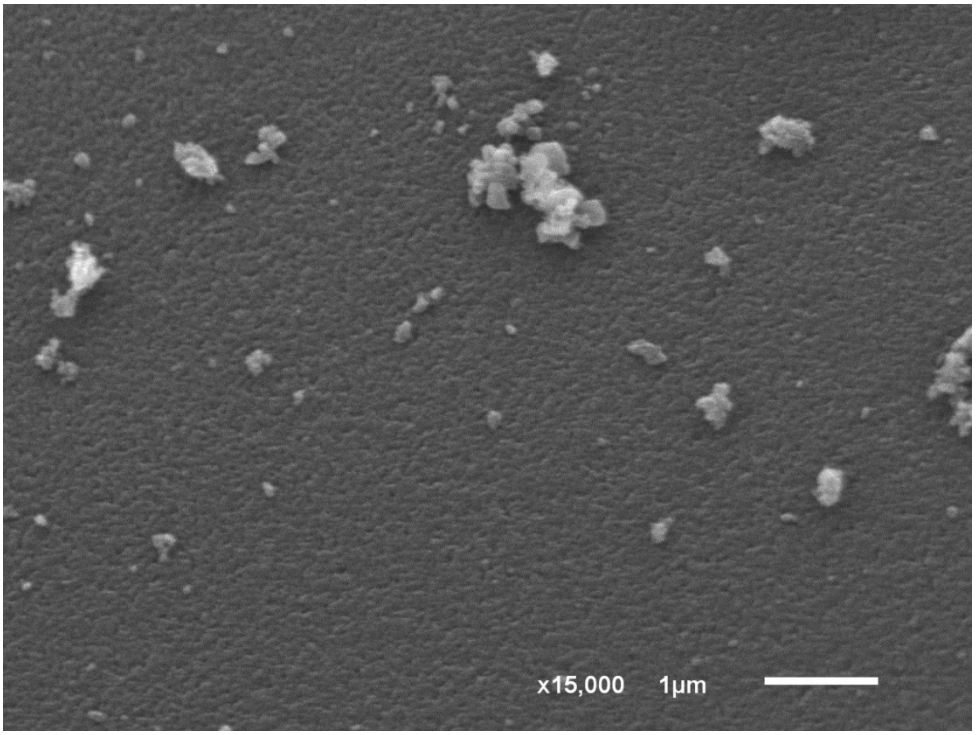

Figure 5.22 SEM of TiC/Al_2O_3 composite (sample 14) - secondary electrons, detail of grain surface (15,000x magnification)

Graph 5.17 Diffraction pattern of $TiC\text{-}Al_2O_3$ mixture (sample 14) – obtained by treating $Al_2O_3/TiO_2/C$ nanocomposite at 1400 °C in argon

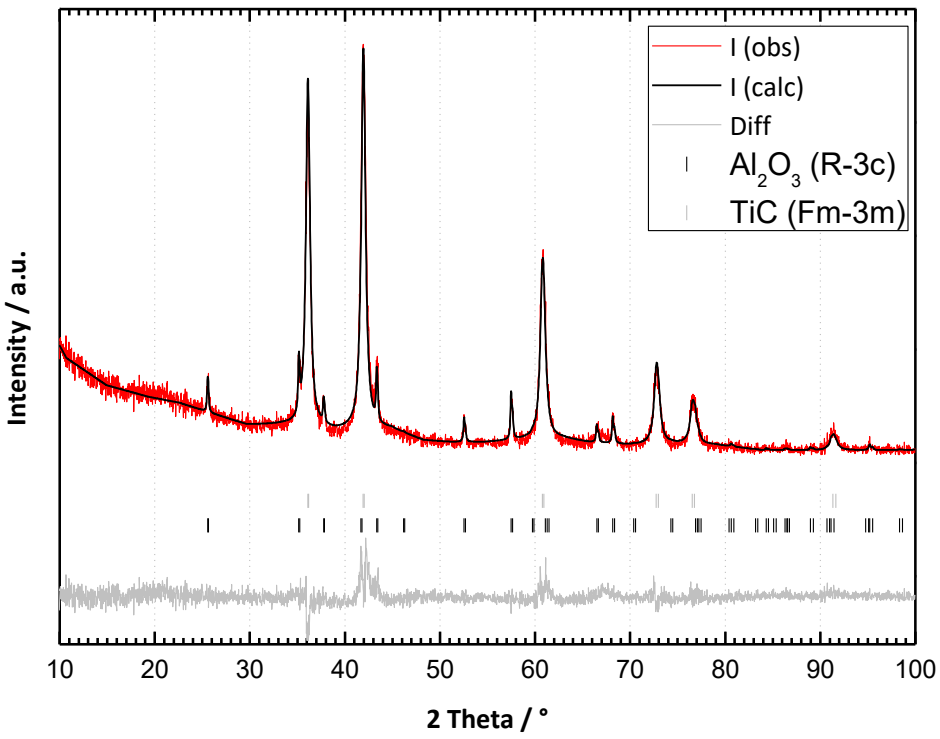

Samples 15 – 18 were synthesized from a precursor – sample 12 (subsection 5.1.3). The purpose of these samples was to show the effects of the final synthesis temperature on the phase composition. As outlined in Table 5.1, the samples were treated at temperatures ranging from 1100 °C to 1400 °C.

PXRD showed that the only phase present in those samples was TiC at temperatures below 1400 °C. Sample 18 treated at 1400 °C (Graph 5.18) contained 2.2% of Al_4C_3, which corresponds to a Ti:Al molar ratio of 26.7. Such a high number does not necessarily mean loss of aluminium, but only a small fraction of the aluminium might have turned into a crystalline carbide phase. In contrast, sample 13 (Ti:Al ratio 5) ,was treated under identical conditions, showed rather poor reproducibility during the SPS process, most likely resulting from reactions with the punches or uptake of particles by the gaseous side-products. The underlying cause is unclear and thus the poor reproducibility could not be resolved within the timeframe of this thesis.

The average apparent size of TiC particles increases with the synthesis temperature. Those sizes are: 7.4 nm for 1100 °C, 9.3 nm for 1200 °C, 10.5 nm for 1300 °C and 14.0 nm for 1400 °C. This increase is manifested as peak broadening, as shown in Graph 5.19 and Graph 5.20. In the case of the Al_4C_3 Phase, in sample 18, the average apparent size could not be calculated due to the limited resolution of the broadening of reflections.

Graph 5.18 Diffraction pattern of TiC-Al_4C_3 mixture (sample 18) – obtained by treating Al_2O_3/TiO_2/C nanocomposite at 1400 °C in vacuum

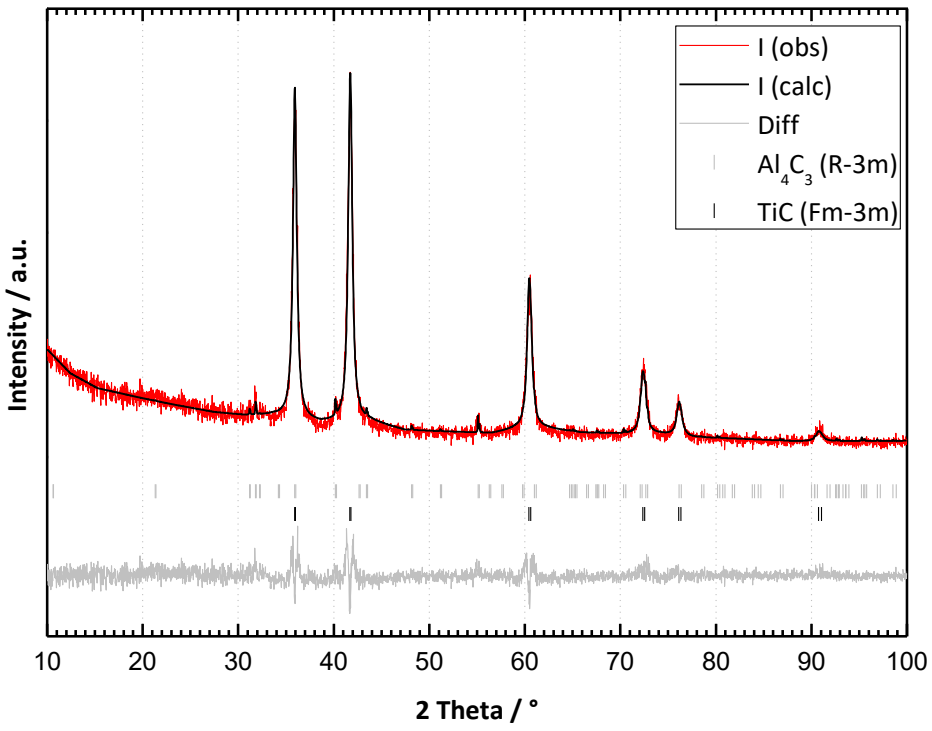

Graph 5.19 Diffraction patterns of TiC (samples 15 - 18) -
obtained by treating $Al_2O_3/TiO_2/C$ nanocomposites at different temperatures in vacuum

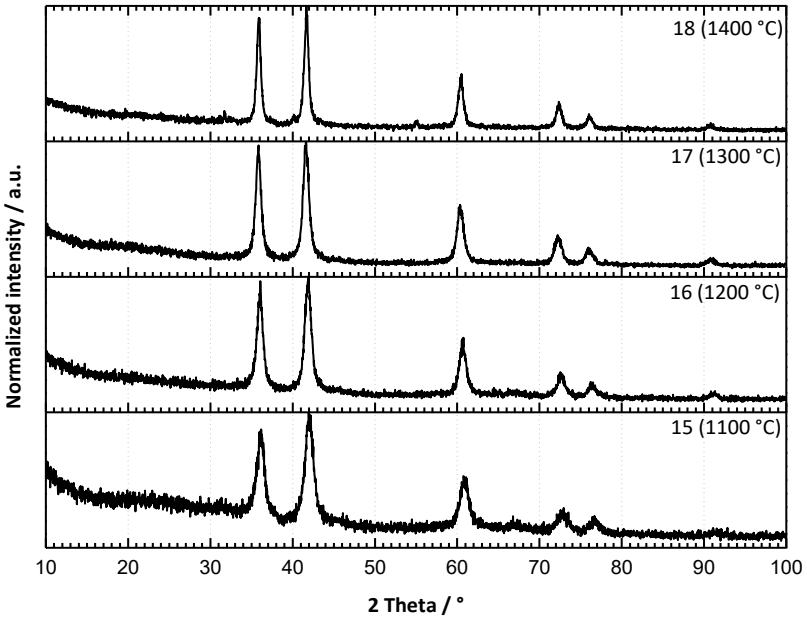

Graph 5.20 Peak broadening caused by decreasing size of TiC nanoparticles (samples 15 -18)

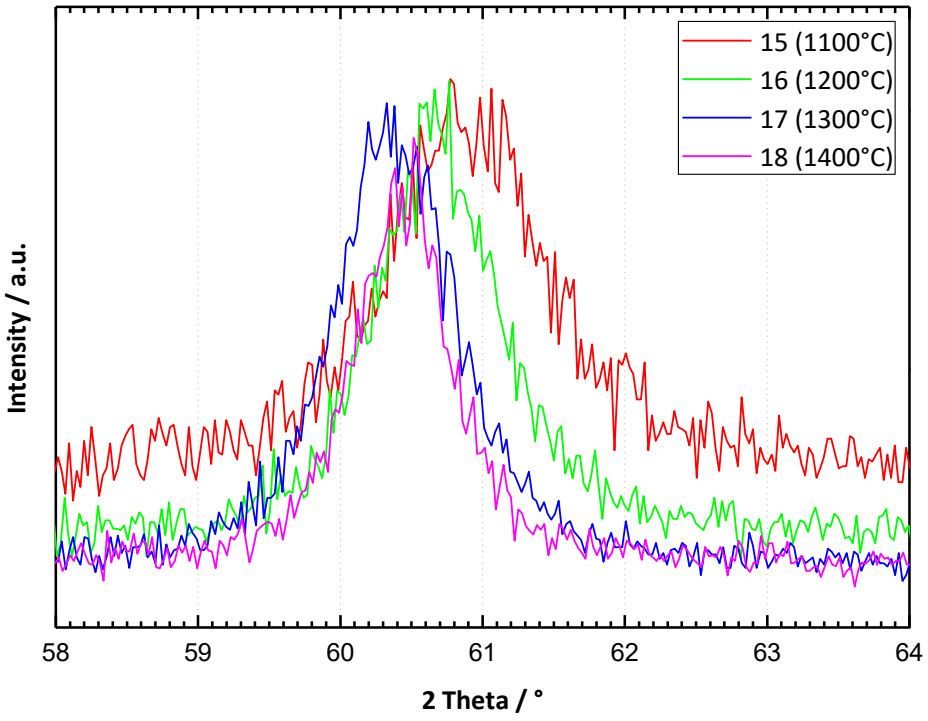

The slower heating rate during the SPS process should decrease the uptake of particles by forming gaseous side-products and thus the composition of sample should remain unchanged throughout the process. Prolonging the heating cycle or increasing the temperature might help to complete the reaction. These heating cycle optimizations are a crucial part of the synthesis of precursors, which are needed to ensure reproducible Ti:Al ratios in any future synthesis attempts.

To my knowledge, no research has been conducted on the synthesis of MAX Phases solely from carbide precursors, thus precluding any assertion as to whether sintering the two-phase carbide samples would yield Ti_2AlC. The effect of increasing the fraction of both titanium and aluminium on the form of carbides has been tested previously [62]. Increasing the fraction of titanium in the form of TiC benefits the synthesis, while aluminium in the form of Al_4C_3 hampers it. Additionally, Łopaciński et al. [63] reported Ti_2AlC MAX Phase decomposition at approximately 1625 °C, yielding TiC and Al_4C_3. Thus, the reaction of those phases forming Ti_2AlC may be difficult.

6 Conclusion

Single-metal aluminium and titanium carbides were successfully synthesized using chloride precursors. The oxide/carbon precursor mixtures used for their synthesis were amorphous or nearly amorphous and lead to total conversion into the respective carbides through SPS treatment. The resulting powders showed small crystallite sizes ranging from 50 to 100 nm.

When attempting mixed-metal carbide synthesis using chloride precursors, most aluminium was lost during precursor preparation. This problem was tackled by adopting a new synthesis route using peroxo-titanate and aluminium nitrate without chloride ions. This new method was partly successful, improving aluminium retention in the sample. The precursors prepared this way had very small crystallite sizes. Aluminium oxide was amorphous and titanium oxide had an average crystallite size of 10 nm. Both oxides were mixed homogeneously inside the active carbon matrix.

The peroxo-titanate synthetic route provided a mixture of aluminium carbide and titanium carbide. To my knowledge, no reports have shown whether the two can react to form Ti_2AlC or any other MAX Phase. The particle sizes of carbides in the mixture varied with the temperature but were generally very small, with Titanium carbide ranging from 7 to 14 nm. Only one sample contained enough crystalline aluminium carbide to asses its size of 16 nm.

7 References

[1] **T. Lapauw, J. Vleugels, and K. Lambrinou**, MAX phase ceramics and methods for producing the same, *WO2016202892A1*, 2016.

[2] **M. W. Barsoum, D. Brodkin, T. El-Raghy, and G. S. Yaroschuk**, Synthesis of h-phase products, *WO199702796 5A1*, 1997.

[3] **M. Barsoum, T. El-Raghy, D. Brodkin, A. Zavaliangos, and S. Kalidindi**, Synthesis of 312 phases and composites thereof, *US5942455A*, 1999.

[4] **P. Finkel, M. W. Barsoum, S. Basu, and A. Zhou**, Method for structural health monitoring using a smart sensor system, *US7917311B2*, 2011.

[5] **T. El-Raghy and M. Barsoum**, MAX phase Glove and Condom Formers, 2004.

[6] **N. Christiansen, R. Küngas, and B. P. G. B. Tullmar**, MAX phase materials for use in solid oxide fuel cells and solid oxide electrolysis cells, *EP2945207A1*, 2015.

[7] **H. O. Pierson**, Handbook of Refractory Carbides & Nitrides: Properties, Characteristics, Processing and Apps. *William Andrew*, 1996.

[8] **C. Schacht**, Refractories Handbook. *CRC Press*, 2004.

[9] **L. Toth**, Transition Metal Carbides and Nitrides, *Academic Press,* 1971.

[10] **D. Salvato *et al.***, Innovative preparation route for uranium carbide using citric acid as a carbon source, *Ceram. Int., vol. 42, no. 15, pp. 16710–16717*, 2016, doi: 10.1016/j.ceramint.2016.07.138.

[11] **B. Matović *et al.***, Synthesis and characterization of hafnium carbide fine powders, *Ceram. Int., vol. 39, no. 1, pp. 719–723*, 2013, doi: 10.1016/j.ceramint.2012.06.083.

[12] **Y. Chen, H. Zhang, H. Ye, and J. Ma**, A simple and novel route to synthesize nano-vanadium carbide using magnesium powders, vanadium pentoxide and different carbon source, *Int. J. Refract. Met. Hard Mater., vol. 29, no. 4, pp. 528–531*, 2011, doi: 10.1016/j.ijrmhm.2011.03.004.

[13] **T. Onoki *et al.***, Synthesis and classification of WC and W metals via organic–inorganic complex precursors, *J. Ceram. Soc. Jpn., vol. 121, no. 1415, pp. 572–574*, 2013, doi: 10.2109/jcersj2.121.572.

[14] **D. Lu *et al.***, Synthesis of ultra-fine hafnium carbide powders combining the methods of liquid precursor conversion and plasma activated sintering, *Ceram. Int., vol. 42, no. 7, pp. 8108–8114*, 2016, doi: 10.1016/j.ceramint.2016.02.012.

[15] **C. Yan, R. Liu, C. Zhang, and Y. Cao**, Zirconium carbide, hafnium carbide and their ternary carbide nanoparticles by an in situ polymerization route, *RSC Adv., vol. 5, no. 46, pp. 36520–36529*, 2015, doi: 10.1039/C4RA14996C.

[16] **C. Yan, R. Liu, Y. Cao, C. Zhang, and D. Zhang**, Synthesis of zirconium carbide powders using chitosan as carbon source, *Ceram. Int., vol. 39, no. 3, pp. 3409–3412*, 2013, doi: 10.1016/j.ceramint.2012.09.032.

[17] **M. Brykala, M. Rogowski, and T. Olczak**, Carbonization of solid uranyl-ascorbate gel as an indirect step of uranium carbide synthesis, *Nukleonika, vol. 60, no. 4, pp. 921–925*, 2015, doi: 10.1515/nuka-2015-0122.

[18] **B. Li, Y.-C. Song, C.-R. Zhang, and J.-S. Yu**, Synthesis and characterization of nanostructured silicon carbide crystal whiskers by sol–gel process and carbothermal reduction, *Ceram. Int., vol. 40, no. 8, Part A, pp. 12613–12616*, 2014, doi: 10.1016/j.ceramint.2014.04.099.

[19] **D. Liu, W.-F. Qiu, T. Cai, Y. Sun, A.-J. Zhao, and T. Zhao**, Synthesis, Characterization, and Microstructure of ZrC/SiC Composite Ceramics via Liquid Precursor Conversion Method, *J. Am. Ceram. Soc., vol. 97, no. 4, pp. 1242–1247*, 2014, doi: 10.1111/jace.12876.

[20] **I. J. McColm**, Dictionary of Ceramic Science and Engineering. *Springer Science & Business Media*, 2013.

[21] **E. K. Storms**, The Refractory Carbides [by] Edmund K. Storms. *Academic Press*, 1967.

[22] **R. Dabouz, M. Bendoumia, L. Belaid, and M. Azzaz**, Dissolution of Al 6%wt c Mixture Using Mechanical Alloying, *Defect Diffus. Forum, vol. 391, pp. 82–87*, 2019, doi: 10.4028/www.scientific.net/DDF.391.82.

[23] **K. Momma and F. Izumi**, VESTA3 for three-dimensional visualization of crystal, volumetric and morphology data*, J. Appl. Crystallogr., 44, 1272-1276*, 2011.

[24] **M. W. Barsoum**, The $M_{N+1}AX_N$ phases: A new class of solids: Thermodynamically stable nanolaminates, *Prog. Solid State Chem., vol. 28, no. 1, pp. 201–281*, 2000, doi: 10.1016/S0079-6786(00)00006-6.

[25] **A.-S. Farle, C. Kwakernaak, S. van der Zwaag, and W. G. Sloof**, A conceptual study into the potential of $M_{n+1}AX_n$-phase ceramics for self-healing of crack damage, *J. Eur. Ceram. Soc., vol. 35, no. 1, pp. 37–45*, 2015, doi: 10.1016/j.jeurceramsoc.2014.08.046.

[26] **S. Kuchida, T. Muranaka, K. Kawashima, K. Inoue, M. Yoshikawa, and J. Akimitsu**, Superconductivity in Lu_2SnC, *Phys. C Supercond., vol. 494, pp. 77–79*, 2013, doi: 10.1016/j.physc.2013.04.050.

[27] **H. Fashandi *et al.***, Synthesis of Ti_3AuC_2, $Ti_3Au_2C_2$ and Ti_3IrC_2 by noble metal substitution reaction in Ti_3SiC_2 for high-temperature-stable Ohmic contacts to SiC, *Nat. Mater., vol. 16, no. 8, pp. 814–818*, 2017, doi: 10.1038/nmat4896.

[28] **H. Ding *et al.***, Synthesis of MAX phases Nb_2CuC and $Ti_2(Al_{0.1}Cu_{0.9})N$ by A-site replacement reaction in molten salts, *Mater. Res. Lett., vol. 7, no. 12, pp. 510–516*, 2019, doi: 10.1080/21663831.2019.1672822.

[29] **P. Eklund, M. Beckers, U. Jansson, H. Högberg, and L. Hultman**, The $M_{n+1}AX_n$ phases: Materials science and thin-film processing, *Thin Solid Films, vol. 518, no. 8, pp. 1851–1878,* 2010, doi: 10.1016/j.tsf.2009.07.184.

[30] **L. Zheng, J. Wang, X. Lu, F. Li, J. Wang, and Y. Zhou**, $(Ti_{0.5}Nb_{0.5})_5AlC_4$: A New-Layered Compound Belonging to MAX Phases, *J. Am. Ceram. Soc., vol. 93, no. 10, pp. 3068–3071*, 2010, doi: 10.1111/j.1551-2916.2010.04056.x.

[31] **J. Emmerlich *et al.***, Thermal stability of Ti_3SiC_2 thin films, *Acta Mater., vol. 55, no. 4, pp. 1479–1488*, 2007, doi: 10.1016/j.actamat.2006.10.010.

[32] **L. Farber and M. W. Barsoum**, 'Isothermal sections in the Cr–Ga–N system in the 650–1000 °C temperature range', *J. Mater. Res., vol. 14, no. 6, pp. 2560–2566,* 1999, doi: 10.1557/JMR.1999.0343.

[33] **R. Radhakrishnan, J. J. Williams, and M. Akinc**, 'Synthesis and high-temperature stability of Ti_3SiC_2', *J. Alloys Compd., vol. 285, no. 1, pp. 85–88,* 1999, doi: 10.1016/S0925-8388(99)00003-1.

[34] **T. El-Raghy, A. Zavaliangos, M. W. Barsoum, and S. R. Kalidindi**, Damage Mechanisms around Hardness Indentations in Ti_3SiC_2, *J. Am. Ceram. Soc., vol. 80, no. 2, pp. 513–516*, 1997, doi: 10.1111/j.1151-2916.1997.tb02861.x.

[35] **M. W. Barsoum, L. Farber, and T. El-Raghy**, 'Dislocations, kink bands, and room-temperature plasticity of Ti_3SiC_2', *Metall. Mater. Trans. A, vol. 30, no. 7, pp. 1727–1738,* 1999, doi: 10.1007/s11661-999-0172-z.

[36] **C. Kwakernaak and W. G. Sloof**, 'Work of adhesion of interfaces between M_2AlC (M = Ti, V, Cr) MAX phases and α-Al_2O_3', *Ceram. Int., vol. 44, no. 18, pp. 23172–23179,* 2018, doi: 10.1016/j.ceramint.2018.09.127.

[37] **T. Lapauw *et al.***, 'Synthesis of the novel Zr_3AlC_2 MAX phase', *J. Eur. Ceram. Soc., vol. 36, no. 3, pp. 943–947,* 2016, doi: 10.1016/j.jeurceramsoc.2015.10.011.

[38] **B. Tunca *et al.***, 'Synthesis and Characterization of Double Solid Solution $(Zr,Ti)_2(Al,Sn)C$ MAX Phase Ceramics', *Inorg. Chem., vol. 58, no. 10, pp. 6669–6683,* 2019, doi: 10.1021/acs.inorgchem.9b00065.

[39] **W. B. Zhou, B. C. Mei, J. Q. Zhu, and X. L. Hong**, 'Rapid synthesis of Ti_2AlC by spark plasma sintering technique', *Mater. Lett., vol. 59, no. 1, pp. 131–134,* 2005, doi: 10.1016/j.matlet.2004.07.052.

[40] **O. Guillon *et al.***, 'Field-Assisted Sintering Technology/Spark Plasma Sintering: Mechanisms, Materials, and Technology Developments', *Adv. Eng. Mater., vol. 16, no. 7, pp. 830–849,* 2014, doi: 10.1002/adem.201300409.

[41] **A. Dash, R. Vaßen, O. Guillon, and J. Gonzalez-Julian**, Molten salt shielded synthesis of oxidation prone materials in air, *Nat. Mater., vol. 18, no. 5, pp. 465–470*, 2019, doi: 10.1038/s41563-019-0328-1.

[42] **W. Tian *et al.***, Synthesis and characterization of Cr_2AlC ceramics prepared by spark plasma sintering, *Mater. Lett., vol. 61, no. 22, pp. 4442–4445*, 2007, doi: 10.1016/j.matlet.2007.02.023.

[43] **J. C. Nappé *et al.***, 'Damages induced by heavy ions in titanium silicon carbide: Effects of nuclear and electronic interactions at room temperature', *Nucl. Mater. III, vol. 385, no. 2, pp. 304–307,* 2009, doi: 10.1016/j.jnucmat.2008.12.018.

[44] **S. Shi, L. Zhang, and J. Li**, 'Ti_3SiC_2 material: An application for electromagnetic interference shielding', *Appl. Phys. Lett., vol. 93, no. 17, p. 172903*, 2008, doi: 10.1063/1.3009200.

[45] **M. Borysiewicz, E. Kamińska, A. Piotrowska, I. Pasternak, R. Jakieła, and E. Dynowska**, 'Ti-Al-N MAX Phase a Candidate for Ohmic Contacts to n-GaN', *Acta Phys. Pol. A, vol. 114, no. 5, pp. 1061–1066,* 2008, doi: 10.12693/APhysPolA.114.1061.

[46] **H. Cordes and Y. A. Chang**, 'Interfacial Reactions and Electrical Properties of Ti/n-GaN Contacts', *MRS Internet J. Nitride Semicond. Res., vol. 2, p. e2,* 1997, doi: 10.1557/S1092578300001289.

[47] **K. R. Anderson, J. R. Groza, M. Fendorf, and C. J. Echer**, 'Surface oxide debonding in field assisted powder sintering', *Mater. Sci. Eng. A, vol. 270, no. 2, pp. 278–282*, 1999, doi: 10.1016/S0921-5093(99)00197-5.

[48] **M. Cologna, B. Rashkova, and R. Raj**, 'Flash sintering of nanograin zirconia in <5 s at 850°C', *J. Am. Ceram. Soc., vol. 93, no. 11, pp. 3556–3559,* 2010, doi: 10.1111/j.1551-2916.2010.04089.x.

[49] **G. Cabouro, S. Chevalier, E. Gaffet, Y. Grin, and F. Bernard**, 'Reactive sintering of molybdenum disilicide by spark plasma sintering from mechanically activated powder mixtures: Processing parameters and properties', *J. Alloys Compd., vol. 465, no. 1, pp. 344–355,* 2008, doi: 10.1016/j.jallcom.2007.10.141.

[50] **F. Zhang, F. Ahmed, J. Bednarcik, and E. Burkel**, 'Diamond synthesis through the generation of plasma during spark plasma sintering', *Phys. Status Solidi Appl. Mater. Sci., vol. 209, no. 11, pp. 2241–2246,* 2012, doi: 10.1002/pssa.201228317.

[51] **Z. A. Munir, U. Anselmi-Tamburini, and M. Ohyanagi**, 'The effect of electric field and pressure on the synthesis and consolidation of materials: A review of the spark plasma sintering method', *J. Mater. Sci., vol. 41, no. 3, pp. 763–777,* 2006, doi: 10.1007/s10853-006-6555-2.

[52] **G. Lihao**, 'Processing of uranium dioxide nuclear fuel pellets using spark plasma sintering', *Disertation thesis, University of Florida, [Gainesville, Fla.]* Florida, 2014.

[53] **Z. Shen, M. Johnsson, Z. Zhao, and M. Nygren**, 'Spark Plasma Sintering of Alumina', *J. Am. Ceram. Soc., vol. 85, no. 8, pp. 1921–1927,* 2002, doi: 10.1111/j.1151-2916.2002.tb00381.x.

[54] **M. Suarez *et al.***, 'Challenges and Opportunities for Spark Plasma Sintering: A Key Technology for a New Generation of Materials', *Sintering Applications*, 2013.

[55] **J. R. Groza and A. Zavaliangos**, 'Sintering activation by external electrical field', *Mater. Sci. Eng. A, vol. 287, no. 2, pp. 171–177*, 2000, doi: 10.1016/S0921-5093(00)00771-1.

[56] 'Solution of Aluminum Citrate', *J. Am. Pharm. Assoc. Pract. Pharm. Ed, vol. 3, no. 4, pp. 134–136*, 1942, doi: 10.1016/S0095-9561(16)30357-7.

[57] **R. Uppal, C. D. Incarvito, K. V. Lakshmi, and A. M. Valentine**, 'Aqueous Spectroscopy and Redox Properties of Carboxylate-Bound Titanium', *Inorg. Chem., vol. 45, no. 4, pp. 1795–1804,* 2006, doi: 10.1021/ic051714j.

[58] **D. Wyrzykowski, E. Hebanowska, G. Nowak-Wiczk, M. Makowski, and L. Chmurzyński**, 'Thermal behaviour of citric acid and isomeric aconitic acids', *J. Therm. Anal. Calorim., vol. 104, no. 2, pp. 731–735,* 2011, doi: 10.1007/s10973-010-1015-2.

[59] **P. Pulišová *et al.***, 'Thermal behaviour of titanium dioxide nanoparticles prepared by precipitation from aqueous solutions', *J. Therm. Anal. Calorim., vol. 101, no. 2, pp. 607–613,* 2010, doi: 10.1007/s10973-010-0893-7.

[60] **T. Degen, M. Sadki, E. Bron, U. König, and G. Nénert**, The HighScore suite; *Powder Diffraction/ Volume 29/ Supplement S2/ December 2014/ pp S13-S18*

[61] **Roisnel, T., Rodriguez-Carvajal, J**. WinPLOTR: a Windows tool for powder diffraction patterns analysis. *Materials Science Forum. 2000, 118-123.*

[62] **C. L. Yeh and Y. G. Shen**, 'Effects of TiC and Al_4C_3 addition on combustion synthesis of Ti_2AlC', *J. Alloys Compd., vol. 470, no. 1, pp. 424–428,* 2009, doi: 10.1016/j.jallcom.2008.02.086.

[63] **M. Łopaciński, J. Puszynski, and J. Lis**, 'Synthesis of Ternary Titanium Aluminum Carbides Using Self-Propagating High-Temperature Synthesis Technique', *J. Am. Ceram. Soc., vol. 84, no. 12, pp. 3051–3053,* 2001, doi: 10.1111/j.1151-2916.2001.tb01138.x.

8 Supplement

8.1 Rietveld refinement data

a and ***c*** are the lattice parameters, **BOV** represents an overall isotropic displacement, L_Y is Lorentzian isotropic size, ***GauSiz*** is isotropic size parameter of Gaussian character and **zero shift** is a sample displacement. **BGP** is a number of points used for linear interpolation background (BG) function. **Tot ref. par.** indicates the total number of refined parameters.

sample 2		
Anatase ($I4_1/amd$)		**Rutile ($P4_2/mnm$)**
***a* [Å]**	3.78593(4)	4.59495(5)
***c* [Å]**	9.5150(1)	2.95952(5)
BOV [Å^2]	1.30(2)	1.36(4)
L_Y [0.01°]	0.136(2)	0.046(3)
GauSiz [0.01°]	0.0493(7)	0.0056(3)
Profile function		
Thompson-Cox-Hastings pseudo-Voigt		
zero shift [0.01°]	0.0732(8)	
BG function	linear interpolation	
BGP	84	
R_f [%]	9.28	
R_{wp} [%]	12.2	
R_{exp} [%]	4.99	
χ^2	5.96	
Tot ref. par.	12	

sample 5	
Al_4C_3 ($R\bar{3}m$)	
***a* [Å]**	3.33783(7)
***c* [Å]**	24.9683(6)
BOV [Å^2]	3.24(6)
L_Y [0.01°]	0.103(1)
Profile function	
Thompson-Cox-Hastings pseudo-Voigt	
zero shift [0.01°]	0.056(8)
BG function	linear interpolation
BGP	35
R_f [%]	4.53
R_{wp} [%]	6.48
R_{exp} [%]	3.13
χ^2	4.28
Tot ref. par.	6

sample 8		
Al_4C_3 ($R\bar{3}m$)		Al_2O_3 ($R\bar{3}c$)
***a* [Å]**	3.33689(4)	4.76102(5)
***c* [Å]**	24.9780(5)	12.9975(2)
BOV [Å²]	3.72(7)	2.92(4)
L_Y **[0.01°]**	0.072(1)	0.0550(8)
Profile function		
Thompson-Cox-Hastings pseudo-Voigt		
zero shift [0.01°]		0.0732(8)
BG function		linear interpolation
BGP		40
R_f **[%]**		5.8
R_{wp} **[%]**		7.9
R_{exp} **[%]**		3.22
χ^2		6.03
Tot ref. par.		11

sample 9	
TiC ($Fm\bar{3}m$)	
***a* [Å]**	4.22958(3)
BOV [Å²]	2.47(6)
L_Y **[0.01°]**	0.0527(5)
Profile function	
Thompson-Cox-Hastings pseudo-Voigt	
zero shift [0.01°]	0.0433(9)
BG function	linear interpolation
BGP	22
R_f **[%]**	13.1
R_{wp} **[%]**	17.7
R_{exp} **[%]**	7.62
χ^2	5.4
Tot ref. par.	5

sample 10	
TiC ($Fm\bar{3}m$)	
***a* [Å]**	4.32779(3)
BOV [Å^2]	0.77(7)
L_Y [0.01°]	0.0326(5)
Profile function	
Thompson-Cox-Hastings pseudo-Voigt	
zero shift [0.01°]	0.1121(8)
BG function	linear interpolation
BGP	36
R_f [%]	17.3
R_{wp} [%]	23.3
R_{exp} [%]	8.67
χ^2	7.16
Tot ref. par.	5

sample 12	
Rutile ($P4_2/mnm$)	
***a* [Å]**	4.5892(5)
***c* [Å]**	2.9566(3)
BOV [Å^2]	3.76(7)
L_Y [0.01°]	0.07(2)
GauSiz [0.01°]	0.49(1)
Profile function	
Thompson-Cox-Hastings pseudo-Voigt	
zero shift [0.01°]	0.056(8)
BG function	linear interpolation
BGP	29
R_f [%]	7.95
R_{wp} [%]	10.5
R_{exp} [%]	9.08
χ^2	1.34
Tot ref. par.	7

sample 13

Al_4C_3 ($R\bar{3}m$)		TiC ($Fm\bar{3}m$)	
***a* [Å]**	3.3330(2)	***a* [Å]**	4.3277(2)
***c* [Å]**	24.945(4)	**BOV [Å²]**	3.27(7)
BOV [Å²]	0.4(3)	L_Y **[0.01°]**	0.479(2)
L_Y **[0.01°]**	0.35(1)		
Profile function			
Thompson-Cox-Hastings pseudo-Voigt			
zero shift [0.01°]		0.048(3)	
BG function		linear interpolation	
BGP		31	
R_f **[%]**		5.8	
R_{wp} **[%]**		7.9	
R_{exp} **[%]**		3.22	
χ^2		6.03	
Tot ref. par.		10	

sample 14

Al_2O_3 ($R\bar{3}c$)		TiC ($Fm\bar{3}m$)	
***a* [Å]**	4.7613(3)	***a* [Å]**	4.3077(3)
***c* [Å]**	12.993(2)	**BOV [Å²]**	2.74(7)
BOV [Å²]	2.0(3)	L_Y **[0.01°]**	0.431(2)
L_Y **[0.01°]**	0.096(4)		
Profile function			
Thompson-Cox-Hastings pseudo-Voigt			
zero shift [0.01°]		0.053(3)	
BG function		linear interpolation	
BGP		25	
R_f **[%]**		10.6	
R_{wp} **[%]**		14.1	
R_{exp} **[%]**		10.76	
χ^2		1.71	
Tot ref. par.		10	

sample 15	
TiC ($Fm\bar{3}m$)	
***a* [Å]**	4.3041(5)
BOV [Å^2]	5.2(2)
L_Y [0.01°]	0.760(6)
Profile function	
Thompson-Cox-Hastings pseudo-Voigt	
zero shift [0.01°]	-0.03(1)
BG function	linear interpolation
BGP	30
R_f [%]	8.37
R_{wp} [%]	11.4
R_{exp} [%]	9.22
χ^2	1.53
Tot ref. par.	5

sample 16	
TiC ($Fm\bar{3}m$)	
***a* [Å]**	4.3168(2)
BOV [Å^2]	3.32(9)
L_Y [0.01°]	0.605(3)
Profile function	
Thompson-Cox-Hastings pseudo-Voigt	
zero shift [0.01°]	-0.013(6)
BG function	linear interpolation
BGP	24
R_f [%]	9.82
R_{wp} [%]	13.3
R_{exp} [%]	10.15
χ^2	1.72
Tot ref. par.	5

sample 17	
TiC ($Fm\bar{3}m$)	
***a* [Å]**	4.3310(2)
BOV [Å^2]	3.16(8)
L_Y [0.01°]	0.536(3)
Profile function	
Thompson-Cox-Hastings pseudo-Voigt	
zero shift [0.01°]	0.07(1)
BG function	linear interpolation
BGP	28
R_f [%]	11.3
R_{wp} [%]	15.5
R_{exp} [%]	11.06
χ^2	1.97
Tot ref. par.	5

sample 18			
Al_4C_3 ($R\bar{3}m$)		**TiC ($Fm\bar{3}m$)**	
***a* [Å]**	3.3307(1)	***a* [Å]**	4.3292(2)
***c* [Å]**	24.980(2)	**BOV [Å^2]**	3.64(9)
BOV [Å^2]	0.020(7)	**L_Y [0.01°]**	0.401(2)
L_Y [0.01°]	0.00007(0)		
Profile function			
Thompson-Cox-Hastings pseudo-Voigt			
zero shift [0.01°]	0.038(4)		
BG function	linear interpolation		
BGP	26		
R_f [%]	9.66		
R_{wp} [%]	13.3		
R_{exp} [%]	10.13		
χ^2	1.73		
Tot ref. par.	10		